

## ABSTRACT

Title of dissertation:      Measuring topology of BECs  
in a synthetic dimensions lattice

Dina Genkina  
Doctor of Philosophy, 2018

Dissertation directed by:   Professor Ian Spielman  
Department of Physics

Measuring topology of BECs in a synthetic dimensions lattice

by

Dina Genkina

Dissertation submitted to the Faculty of the Graduate School of the  
University of Maryland, College Park in partial fulfillment  
of the requirements for the degree of  
Doctor of Philosophy  
2018

Advisory Committee:  
Professor Ian Spielman, Chair/Advisor

© Copyright by  
Dina Genkina  
2018



# Table of Contents

List of Tables	6
List of Figures	7
2 Introduction	1
2.1 Bose-Einstein condensation . . . . .	1
2.1.1 Phase transition of a non-interacting Bose gas . . . . .	1
2.1.2 Interacting Bose gas . . . . .	6
2.2 Degenerate Fermi Gas . . . . .	10
2.2.1 Fermi statistics and the onset of degeneracy . . . . .	10
2.2.2 Interactions and Feshbach resonances . . . . .	12
2.3 RbK apparatus . . . . .	14
3 Atom Light Interactions	16
3.1 Near-resonant atom-light interaction . . . . .	16
3.2 Absorption imaging . . . . .	17
3.2.1 Time-of-flight and in situ imaing . . . . .	20
3.3 One dimensional optical lattices . . . . .	21
3.3.1 Far off-resonant atom-light interaction . . . . .	21
3.3.2 Lattice Hamiltonian . . . . .	23
3.3.3 Tight binding approximation . . . . .	26
3.3.4 Pulsing vs adiabatic loading of the lattice . . . . .	27
3.4 Raman and rf coupling . . . . .	31
3.4.1 Hyperfine structure . . . . .	31
3.4.2 Rf coupling Hamiltonian . . . . .	34
3.4.3 Raman coupling Hamiltonian . . . . .	36
3.4.4 Calibration of Raman and Rf dressed states . . . . .	39
Bibliography	45

## List of Tables

## List of Figures

1	Occupation of energy states of a 3-D harmonic oscillator. The trapping frequencies are $\omega_x = \omega_y = \omega_z = 2\pi 50$ Hz, and the atom number is $N = 10^6$ . Dots represent the total fractional population in 50 adjacent energy levels, including degeneracies. The stars represent the fractional population in just the ground state. . . . .	4
2	Time-of-flight images of atoms. (a) Above the critical temperature - the atoms are thermally distributed. (b) Below the critical temperature - about half of the atoms are condensed in the central peak. (c) Far below the critical temperature - almost all atoms are condensed in the central peak. . . . .	5
3	In situ measurement of a fraction of bose condensed atoms. (a) Absorption image taken of $\approx 1\%$ of the cloud. The $x$ and $y$ axes represent $x$ and $y$ position, while color represents the atom number. (b) The blue line represents atom number as a function of position along the $x$ axis, integrated over the $y$ axis. The black dashed line represents the best fit of a Gaussian function to the atomic distribution. The dashed red line represents the best fit of a Thomas-Fermi profile to the atomic distribution. . . . .	9
4	Occupation number as a function of energy for a Fermi gas of $N = 10^6$ atoms in a 3-D harmonic oscillator with frequencies $\omega_x = \omega_y = \omega_z = 2\pi 50$ Hz. The Fermi temperature for these parameters is $T_F = 436$ nK. 12	
5	Schematic of a Feshbach resonance. (a) Energy of Figure taken from [?]. 13	
1	Absorption imaging. (a) Near resonant probe light illuminates the atoms, and the transmitted light (containing a shadow of the atoms) is imaged on the camera. A second image taken with no atoms provides a reference. (b) The probe beam is partially absorbed as it traverses the cloud, and the intensity seen by atoms further along the imaging direction $e_z$ is lowered. (c) An atomic cloud illuminated by a probe light field absorbs photons from the probe and re-emits them in all directions. This process results in a net acceleration of the cloud in the direction of the probe light as well as diffusive spreading in the transverse directions. . . . .	18

2	Lattice band structure in the extended zone scheme. The dashed lines represent the limit of zero lattice depth, with the regular parabolic dispersion relation of a free particle repeating with reciprocal lattice period. The solid lines are the dispersion relation at $V_0 = 4.0E_L$ , showing the opening of gaps at crossings of the zero lattice depth bands. The black lines demarcate the first Brillouin zone. . . . .	25
3	Lattice pulsing. (a) Lattice depth as a function of time during a pulsing experiment. The lattice is turned on instantaneously at $t = 0$ and held on for a variable amount of time until being turned off instantaneously at a final time $t = t_f$ . (b) Atomic population before $t = 0$ . The dispersion relation is that of a free particle, and all of the atoms start out at $q = 0$ in the lowest energy level. Here, the area of the dots is proportional to the fractional population in the energy state. (c) Atomic population after the lattice is turned on for a lattice depth of $V_0 = 8.0E_L$ . The energy spectrum now shows the lattice band structure, and some atomic population is projected onto the excited bands. (d) Atomic population after the lattice is snapped off at $t_f = 150 \mu s$ . The wavefunction is projected back onto the bare states, with some fraction (blue circle) in the lowest band at $k = 0$ and some fraction in the excited band, with equal population being projected onto the $k = 2k_L$ (green) and $k = -2k_L$ (red). . . . .	29
4	Lattice pulsing for calibration. (a) An example time-of-flight image from a pulsing experiment. The three different clouds are different momentum orders. (b) Fractional populations in the different momentum orders as a function of pulsing time at a low lattice power. Data is indicated by dots and best fit theory is represented by lines. The lattice depth from fit is $V_0 = 5.57 \pm 0.07E_L$ . (c) Fractional populations in the different momentum orders as a function of pulsing time at a higher lattice power. Data is indicated by dots and best fit theory is represented by lines. The lattice depth from fit is $V_0 = 12.69 \pm 0.07E_L$ . . . . .	30
5	Adiabatic lattice loading. (a) Lattice depth as a function of time during adiabatic turn-on. The lattice is ramped on starting at $t = 0$ , slowly increasing to a final lattice depth and turned off instantaneously at a final time $t = t_f$ . (b) Atomic population before $t = 0$ . All atoms are at $k = 0$ in the lowest bare band. (c) Atomic population after the lattice is turned on adiabatically to a lattice depth of $V_0 = 8.0E_L$ . All atoms remain in the lowest band, but the band is no longer bare. (d) Atomic population after the lattice is snapped off. The wavefunction is projected back onto the bare states, with some fraction (blue circle) in the lowest band at $k = 0$ and some fraction in the excited band, with equal population being projected onto the $k = 2k_L$ (green) and $k = -2k_L$ (red). Since the lowest lattice band is a superposition of bare bands, some atoms are excited to the higher bare bands. . . . .	32



6	Energy structure of hyperfine states of the ground state of $^{87}\text{Rb}$ as a function of external magnetic field strength in Gauss. Figure from ref. [1] . . . . .	33
7	Raman and rf coupling schematic. (a) Beam geometry of the Raman beams and rf relative to the external field. The Raman beams have a frequency difference $\Delta\omega$ , and are linearly polarized in perpendicular directions. (b) Level structure of both Raman and Rf coupling for hyperfine states of the $F = 1$ manifold. The hyperfine splitting separates the levels by an energy $\hbar\omega_z$ . The quadratic Zeeman shift $\epsilon$ lowers the energy of the $m_F = 0$ state, and the detuning $\delta$ of either the Raman or the rf fields shifts the energies of the $m_F = \pm 1$ states. Raman transitions are two-photon, exciting up to a virtual state and coming back down to an adjacent hyperfine state, with an accompanying momentum transfer. Rf couples adjacent hyperfine states directly. Figure taken from ref. [2] . . . . .	35
8	Band structure of the rf Hamiltonian, Eq. 3.28, in momentum space. For all plots, the quadratic Zeeman shift $\hbar\epsilon = 0.04E_R$ , and the color represents magnetization, labeled by the colorbar. (a) $\hbar\Omega = 0$ , $\hbar\delta = 0$ . No coupling or detuning is present, so the only separation between the bands is due to the quadratic shift $\hbar\epsilon$ . (b) $\hbar\Omega = 5.0E_R$ , $\hbar\delta = 0$ . (c) $\hbar\Omega = 0$ , $\hbar\delta = 1.0E_R$ . Even though the coupling strength is zero, the bands are separated by the detuning. (d) $\hbar\Omega = 5.0E_R$ , $\hbar\delta = 1.0E_R$ . . . . .	37
9	Band structure of the Raman Hamiltonian, Eq. 3.31, in momentum space. For all plots, the quadratic Zeeman shift $\hbar\epsilon = 0.04E_R$ , and the color represents magnetization, labeled by the colorbar. (a) $\hbar\Omega = 0$ , $\hbar\delta = 0$ . (b) $\hbar\Omega = 1.0E_R$ , $\hbar\delta = 0$ . (c) $\hbar\Omega = 5.0E_R$ , $\hbar\delta = 0.0$ . (d) $\hbar\Omega = 0.0$ , $\hbar\delta = 1.0E_R$ . (e) $\hbar\Omega = 1.0E_R$ , $\hbar\delta = 1.0E_R$ . (f) $\hbar\Omega = 5.0E_R$ , $\hbar\delta = 1.0E_R$ . . . . .	40
10	Pulsing on rf coupling. (a) Example time-of-flight image during an rf pulsing experiment in the $F = 1$ manifold. Spin states are separated via a Stern-Gerlach pulse along the horizontal direction. (b) Example time-of-flight image during an rf pulsing experiment in the $F = 2$ manifold. Here, 5 spin components are present. (c) Pulsing experiment in the $F = 1$ manifold. Dots represent fractional populations in different spin states measured from time-of-flight images, and lines represent best fit theory curves. Fitted parameters are $\hbar\Omega = 0.863 \pm 0.004E_R$ , $\hbar\delta = -0.198 \pm 0.007E_R$ . (d) Pulsing experiment in the $F = 2$ manifold. Dots represent fractional populations in different spin states measured from time-of-flight images, and lines represent best fit theory curves. Fitted parameters are $\hbar\Omega = 1.000 \pm 0.002E_R$ , $\hbar\delta = -0.061 \pm 0.001E_R$ . $\hbar\epsilon = 0.038E_R$ for all panels. . . . .	42

11	Pulsing on Raman coupling. (a) Example time-of-flight image during a Raman pulsing experiment in the $F = 1$ manifold. A Stern-Gerlach pulse during time-of-flight separates different spin components along the horizontal direction, and different momentum orders fly apart along the vertical direction. (b) Fractional population in different spin states during a Raman pulsing experiment as a function of time. Dots represent data and lines represent a best fit from theory. The fitted parameters are $\hbar\Omega = 1.47 \pm 0.01E_R$ , $\hbar\delta = 0.004 \pm 0.024E_R$ . The quadratic Zeeman shift was $\hbar\epsilon = 0.038E_R$ . . . . .	43
----	--	----

## Chapter 2: Introduction

### 2.1 Bose-Einstein condensation

#### 2.1.1 Phase transition of a non-interacting Bose gas

Bose gases are characterized by the Bose-Einstein distribution giving the number of atoms  $n(E_j)$  occupying each energy eigenstate  $E_j$  as

$$n(E_j) = \frac{1}{e^{(E_j - \mu)/k_B T} - 1}, \quad (2.1)$$

where  $k_B$  is the Boltzmann constant,  $T$  is the temperature in Kelvin,  $\mu$  is the chemical potential. Assuming the total atom number  $N$  is fixed, the chemical potential  $\mu(T, N)$  ensures that the total occupation of all  $\sum_j n(E_j) = N$ .

The Bose distribution leads to Bose-Einstein condensation, the collapse of a macroscopic fraction of the atoms into the ground state. This comes as a direct consequence of the Bose distribution's characteristic  $-1$  in the denominator. Consider the occupation number  $n(E_j)$ —it must remain positive, as a negative occupation number is unphysical. That means that the quantity  $e^{(E_j - \mu)/k_B T}$  must remain greater than 1, or  $(E_j - \mu)/k_B T < 0$  for all  $E_j$ . Therefore,  $\mu \leq E_0$ , where  $E_0$  is the ground state energy.

Then, for a given temperature  $T$ , there is a maximum occupation number for each excited state given by  $n(E_j) = \frac{1}{e^{E_j/k_B T} - 1}$ . The only energy state whose occupation number is unbounded is the ground state, as  $n(E_0)$  tends toward infinity as  $\mu$

tends towards 0. Therefore, as the temperature decreases, the maximum occupation of each excited state decreases until they can no longer support all of the atoms. The remaining atoms then have no choice but to collapse into the lowest energy level and Bose condense.

We will show this quantitatively for the case of a 3-D harmonically trapped gas of atoms, relevant to the experiments described in this thesis. It is convenient to define the fugacity  $\zeta = e^{\mu/k_B T}$ , and re-write the Bose-Einstein distribution as eigenstate  $E_j$  as

$$n(E_j) = \frac{\zeta}{e^{E_j/k_B T} - \zeta}. \quad (2.2)$$

The harmonic oscillator potential can be written as

$$V(r) = \frac{1}{2}m(\omega_x^2 x^2 + \omega_y^2 y^2 + \omega_z^2 z^2), \quad (2.3)$$

where  $\omega_x$ ,  $\omega_y$  and  $\omega_z$  are the angular trapping frequencies along  $\mathbf{e}_x$ ,  $\mathbf{e}_y$ , and  $\mathbf{e}_z$ . The eigenenergies with this potential are

$$E(j_x, j_y, j_z) = \left(\frac{1}{2} + j_x\right)\hbar\omega_x + \left(\frac{1}{2} + j_y\right)\hbar\omega_y + \left(\frac{1}{2} + j_z\right)\hbar\omega_z. \quad (2.4)$$

In order to find  $\mu$ , we must find  $\sum_{j_x, j_y, j_z} n(E(j_x, j_y, j_z))$  and set it equal to  $N$ . This task is greatly simplified by going to the continuum limit and finding the density of states. To do this, we neglect the zero-point energy (setting  $E_0 = 0$ , the effects of the zero-point energy are discussed in [3] section 2.5) and assume there is on average one state per volume element  $\hbar^3\omega_x\omega_y\omega_z$ . Then, the total number of states with energy less than or equal to some value  $\epsilon$  is given by the volume of a prism made between points  $(x, y, z) = (0, 0, 0)$ ,  $(\epsilon, 0, 0)$ ,  $(0, \epsilon, 0)$  and  $(0, 0, \epsilon)$  in units of the volume element:

$$G(\epsilon) = \frac{\epsilon^3}{6\hbar^3\omega_x\omega_y\omega_z}. \quad (2.5)$$

The density of states is given by

$$g(\epsilon) = \frac{d}{d\epsilon}G(\epsilon) = \frac{\epsilon^2}{3\hbar^3\omega_x\omega_y\omega_z}. \quad (2.6)$$

Note that the occupation of the ground state is not included in this continuum picture. We can therefore use it only to calculate the total number of atoms in all of the excited states:

$$N_{\text{ex}} = \int_0^\infty d\epsilon g(\epsilon)n(\epsilon) = \int_0^\infty d\epsilon \frac{\epsilon^2}{3\hbar\omega_x\omega_y\omega_z} \frac{\zeta}{e^{\epsilon/k_B T} - \zeta} = \frac{(k_B T)^3}{\hbar^3\omega_x\omega_y\omega_z} \text{Li}_3(\zeta), \quad (2.7)$$

where  $\text{Li}_3(\zeta)$  is the polylogarithm function<sup>1</sup>. We define the mean trapping frequency  $\bar{\omega} = (\omega_x\omega_y\omega_z)^{1/3}$  and the harmonic oscillator energy as  $\hbar\bar{\omega}$ , with the thermal energy in harmonic oscillator units  $\tau = k_B T/\hbar\bar{\omega}$ , giving

$$N_{\text{ex}} = \tau^3 \text{Li}_3(\zeta). \quad (2.8)$$

Finding the occupation number of the ground state from the Bose-Einstein distribution

$$N_0 = \frac{\zeta}{1 - \zeta}, \quad (2.9)$$

we can then find the chemical potential, or equivalently the fugacity  $\zeta$ , to satisfy

$$N = N_0 + N_{\text{ex}}. \quad (2.10)$$

This is a transcendental equation that can only be solved numerically. We present an example of the solution in Figure 1. Here, we have calculated the fractional population in different harmonic oscillator energy levels for three different temperatures, using trapping frequencies are  $\omega_x = \omega_y = \omega_z = 2\pi 50$  Hz, and atom number  $N = 10^6$ .

---

<sup>1</sup>This calculation was done with Wolfram Alpha, not Russian algebra skills

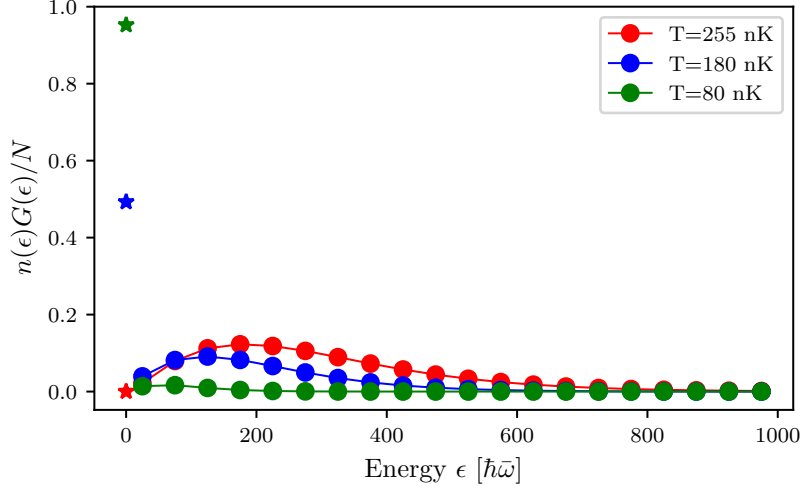


Figure 1: Occupation of energy states of a 3-D harmonic oscillator. The trapping frequencies are  $\omega_x = \omega_y = \omega_z = 2\pi 50$  Hz, and the atom number is  $N = 10^6$ . Dots represent the total fractional population in 50 adjacent energy levels, including degeneracies. The stars represent the fractional population in just the ground state.

For energies above the ground state (dots in the figure), we binned 50 energy levels together, such that each dot represents the total fractional population in 50 adjacent levels. This was obtained by integrating eqn. 2.7 from  $\epsilon - 25\hbar\omega$  to  $\epsilon + 25\hbar\omega$ . The stars represent the fractional population in just the ground state, calculated from eqn. 2.9. Note that at temperature  $T = 255$  nK (red), the ground state population is consistent with a continuous extrapolation from the excited state populations and is almost zero. At lower temperatures,  $T = 180$  nK (blue) the ground state population is in excess of any reasonable extrapolation from the excited state fractions, and at  $T = 80$  nK (green) almost all the atoms are in the ground state.

The onset of Bose-Einstein condensation occurs at a critical temperature  $T_c$ . This temperature is defined as the temperature at which the occupation number of excited states is equal to the atom number, ie when the atoms have occupied all available excited states and any remaining atoms will have to pile into the ground state. Since the maximal occupation of the excited states will occur at  $\mu = 0$ ,

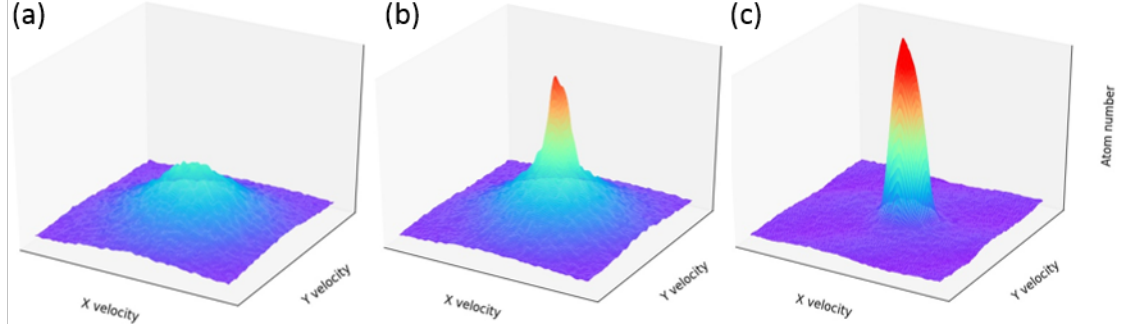


Figure 2: Time-of-flight images of atoms. (a) Above the critical temperature - the atoms are thermally distributed. (b) Below the critical temperature - about half of the atoms are condensed in the central peak. (c) Far below the critical temperature - almost all atoms are condensed in the central peak.

the occupation of the excited state is bounded from above by  $N_{\text{ex}}(\mu = 0)$ , and the critical temperature is defined by

$$N = N_{\text{ex}}(\mu = 0, T = T_c) = \frac{(k_B T_c)^3}{\hbar^3 \omega_x \omega_y \omega_z} Li_3(\zeta = 1). \quad (2.11)$$

Using  $Li_3(1) \approx 1.202$ , we obtain for a given atom number and trapping frequencies

$$T_c = \frac{1.202 N}{k_B^3} \hbar^3 \omega_x \omega_y \omega_z. \quad (2.12)$$

For the parameters in Figure 1,  $T_c = 225$  nK.

For temperatures below the critical temperature, the condensation fraction  $f_c$ —the fraction of atoms in the ground state—is directly related to the ratio of the temperature to the critical temperature:

$$f_c = 1 - \frac{N}{N_{\text{ex}}} = 1 - \frac{(k_B T)^3}{\hbar^3 \omega_x \omega_y \omega_z} Li_3(\zeta = 1) = 1 - \left( \frac{T}{T_c} \right)^3, \quad (2.13)$$

where in the last step we have plugged in the definition of the critical temperature eqn. 2.12.

Figure 2 shows the progression towards condensation as the temperature of a

cloud of  $^{87}\text{Rb}$  is decreased below  $T_c$ . The images are obtained via a time-of-flight measurement (see section 3.2.1), where the atoms are allowed to expand freely, mapping the initial momentum to final position, imaged via absorption imaging (see section 3.2). The  $x$  and  $y$  axes represent momentum along  $x$  and  $y$ , while the  $z$  axis represents the number of atoms. The  $z$  axis momentum is integrated over. Figure 2a shows a cloud above the condensation temperature - the momentum distribution is gaussian, given by the Maxwell-Boltzmann distribution. In fig. 2b, the temperature has been decreased below  $T_c$ , and about half the atoms have collapsed into the ground state, producing a large peak in atom number around zero momentum. In fig. 2c, the temperature has been decreased even further and almost all the atoms populate the central peak - the distribution is no longer gaussian but a sharp peak around zero momentum.

### 2.1.2 Interacting Bose gas

In the previous section, we assumed there was no interaction between the atoms other than that enforced by statistics. In this section, we will relax this assumption somewhat and describe the condensed atomic state through its characteristic Gross-Pitaevskii equation.

Since condensation occurs at very low temperatures, and thus very low kinetic energies, we can assume that any scattering processes between the atoms are  $s$ -wave and can be described simply by a scattering length  $a$ . For  $^{87}\text{Rb}$ , relevant to experiments described in this thesis, the scattering length between two atoms in the  $F = 2$  hyperfine state is  $a = 95.44(7)a_0$  [4], where  $a_0 = 5.29 \times 10^{-11}$  m is the Bohr radius. The short-range interaction between two particles can be approximated as a contact interaction with an effective strength  $U_0$  as (see [3] section 5.2.1):

$$U(r_1, r_2) = U_0 \delta(r_1 - r_2) = \frac{4\pi\hbar^2 a}{m} \delta(r_1 - r_2), \quad (2.14)$$



where  $m$  is the atomic mass and  $\delta$  is the Dirac delta function. The full Hamiltonian of the many-body system is then

$$H = \sum_i \frac{p_i^2}{2m} + V(r_i) + U_0 \sum_{i < j} \delta(r_i - r_j), \quad (2.15)$$

where  $i$  labels the particles,  $p_i$  is the momentum,  $r_i$  is the position, and  $V$  is the external potential.

We make the mean field approximation by assuming that no interactions between two atoms take them out of the ground state, and hence all atoms can be assumed to be in the same single particle wavefunction, making the overall wavefunction

$$\Psi(r_1, r_2, \dots, r_N) = \prod_i^N \phi(r_i), \quad (2.16)$$

where  $\phi$  is the single particle wavefunction. It is convenient to define the wavefunction of the condensed state,  $\psi(r) = \sqrt{N}\phi(r)$ , making the normalization  $N = \int dr |\psi(r)|^2$ .

The energy of this wavefunction under the Hamiltonian above is given by

$$E = \int dr \left[ \frac{\hbar^2}{2m} |\nabla \psi(r)|^2 + V(r) |\psi(r)|^2 + \frac{1}{2} U_0 |\psi(r)|^4 \right] \quad (2.17)$$

Given  $N$  particles, there are  $N(N-1)/2$  unique pairs of particles that can have a pairwise interaction, approximately equal to  $N^2/2$  for large  $N$ . The  $N^2$  is absorbed into the definition of  $\psi$ , but the factor of  $1/2$  remains on the final interaction term. The task of finding the condensed eigenstate reduces to minimizing this energy under the normalization constraint  $N = \int dr |\psi(r)|^2$ . This can be done by using the method of Lagrange multipliers to minimize  $E - \mu N$ . Then, we can minimize this quantity by finding the point where the derivative with respect to  $\psi$  and  $\psi^*$  is zero.

Taking the derivative with respect to  $\psi^*$  we obtain

$$-\frac{\hbar^2}{2m}\nabla^2\psi(r) + V(r)\psi(r) + U_0|\psi(r)|^2\psi(r) = \mu\psi(r), \quad (2.18)$$

which is the Gross-Pitaevskii equation. This is a non-linear equation that generally needs to be solved numerically.

There is another approximation that can be made in cases where the atomic density is high enough that the interaction energy is significantly larger than the kinetic energy. Then, the kinetic term in the Hamiltonian can be neglected. This is called the Thomas-Fermi approximation. Then, the wavefunction is given simply by

$$|\psi(r)|^2 = \frac{\mu - V(r)}{U_0}. \quad (2.19)$$

In this approximation, the probability density simply takes the form of the inverse of the potential. In the case of a harmonically trapped BEC, it is shaped like an inverted parabola. The Thomas-Fermi radius, ie the extent of the particle wavefunction, is the point where the probability density goes to zero:  $\mu - V(r_0) = 0$ . For a harmonic trap, along any direction, this is given by  $r_0^2 = 2\mu/m\omega^2$ .

Figure 3a shows an absorption image of a small fraction of a BEC in situ (see section 3.2.1), meaning as they are in the trap - without expanding in time-of-flight. Therefore, the  $x$  and  $y$  axis represent position, while color represents the atom number. Figure 3b shows the atom number integrated over the  $y$ -axis in blue. The red dashed lines represent a best fit line to a Thomas-Fermi distribution, here an inverse parabola. The black dashed lines represent a best fit of a Gaussian to the atomic distribution. The Thomas-Fermi distribution matches the atomic distribution more closely in the center where the density is high, but the Gaussian distribution does a better job at the tails of the distribution. This is due to the presence of some thermal atoms, which remain Maxwell-Boltzmann distributed.

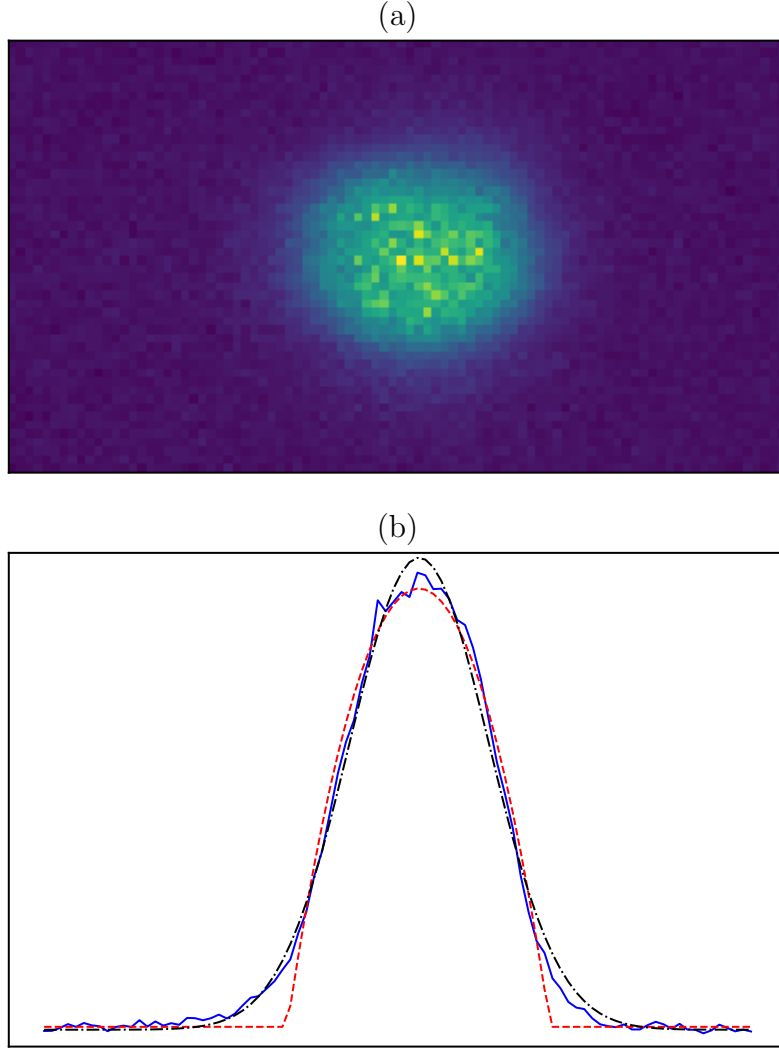


Figure 3: In situ measurement of a fraction of bose condensed atoms. (a) Absorption image taken of  $\approx 1\%$  of the cloud. The  $x$  and  $y$  axes represent  $x$  and  $y$  position, while color represents the atom number. (b) The blue line represents atom number as a function of position along the  $x$  axis, integrated over the  $y$  axis. The black dashed line represents the best fit of a Gaussian function to the atomic distribution. The dashed red line represents the best fit of a Thomas-Fermi profile to the atomic distribution.

## 2.2 Degenerate Fermi Gas

### 2.2.1 Fermi statistics and the onset of degeneracy

The occupation of different energy levels by Fermions is given by the Fermi-Dirac distribution:

$$n(\epsilon) = \frac{1}{e^{(\epsilon-\mu)/k_B T} + 1}. \quad (2.20)$$

The difference from the Bose-Einstein distribution is simply the sign of the 1 in the denominator. This has important implications, however. First, since  $e^x$  varies between 0 and  $\infty$ , the occupation  $n(\epsilon)$  varies between 1 and 0 - a consequence of the Pauli exclusion principle. Second, as the temperature  $T$  tends towards 0, there become two distinct cases:  $\epsilon - \mu > 0$  and  $\epsilon - \mu < 0$ . If  $\epsilon - \mu > 0$ ,  $e^{(\epsilon-\mu)/k_B T}$  tends towards  $\infty$ , and  $n(\epsilon)$  tends towards 0. If  $\epsilon - \mu < 0$ ,  $e^{(\epsilon-\mu)/k_B T}$  tends towards 0, and  $n(\epsilon)$  tends towards 1. Therefore, at  $T = 0$ , the energy states below the chemical potential  $\mu$  are maximally occupied (with probability 1) and the energy states above the chemical potential are unoccupied.

We can use this to determine the chemical potential at  $T = 0$  by constraining the total atom number:

$$N = \sum_j n(E_j) = \sum_{\epsilon_j < \mu} 1. \quad (2.21)$$

Again, we take the common example of the 3-D harmonic trap. Then the task reduces to simply finding the number of energy levels at or below a certain energy  $\mu$ . This is given by eqn. [2.5](#). From this, we find the chemical potential at zero energy, which is known as the Fermi energy  $E_F$ , as

$$E_F = (6N)^{1/3} \hbar \bar{\omega}, \quad (2.22)$$

where  $\bar{\omega} = (\omega_x \omega_y \omega_z)^{1/3}$  is the geometric mean of the three trapping frequencies.

From the Fermi energy, we can define the associated Fermi temperature  $T_F$  as

$$T_F = \frac{(6N)^{1/3} \hbar \bar{\omega}}{k_B}, \quad (2.23)$$

and the Fermi momentum  $\hbar k_F$  as

$$\hbar k_F = \sqrt{2mE_F}, \quad (2.24)$$

where  $m$  is the mass of the Fermion.

For higher temperatures, we can solve for the chemical potential, or the fugacity  $\zeta$ , by integrating the Fermi-Dirac distribution weighted by the density of states (eqn. 2.6) to obtain

$$N = \int_0^\infty \frac{\epsilon^2}{2\hbar^3 \bar{\omega}^3} \frac{\zeta}{e^{\epsilon/k_B T} + \zeta} = -\frac{(k_B T)^3}{\hbar^3 \bar{\omega}^3} Li_3(-\zeta), \quad (2.25)$$

where  $Li_3$  is again the polylogarithm function. Again, this is a transcendental equation that can be solved numerically. However, in contrast to the BEC case, we do not have to consider the ground state occupation separately, as it is bounded by 1 like every other state.

We show an example of the occupation distribution for different temperatures in Figure 5. Here, we have used the same parameter values as for the BEC case:  $N = 10^6$  and  $\omega_x = \omega_y = \omega_z = 2\pi 50$  Hz. The Fermi temperature for these parameters is  $T_F = 436$  nK. For illustrative purposes, we plot  $n(\epsilon)$ , unweighted by the density of states  $g(\epsilon)$ . At zero temperature (red line in the figure), only states below the Fermi energy are occupied. At higher temperatures, the distribution is smoothed out (green and orange lines) until at the Fermi temperature there is almost no significance to the Fermi energy.

In contrast with Bose-Einstein condensation, the transition to a Degenerate

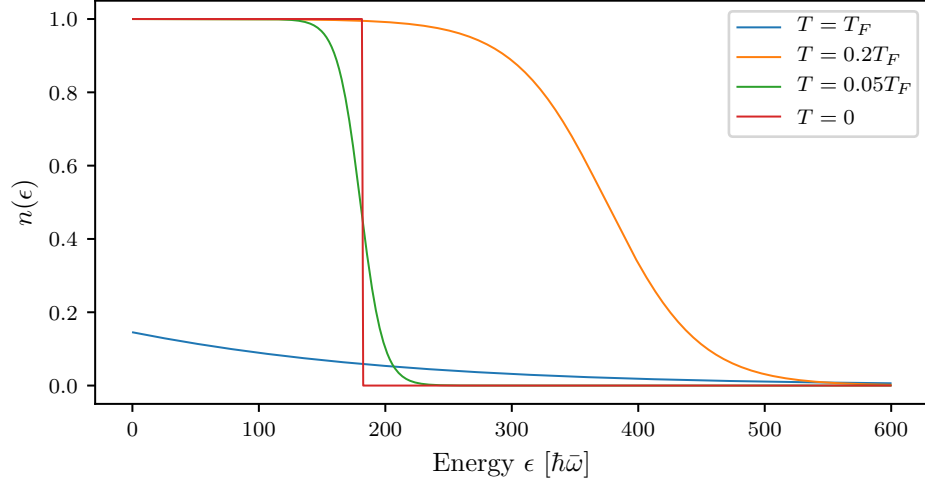


Figure 4: Occupation number as a function of energy for a Fermi gas of  $N = 10^6$  atoms in a 3-D harmonic oscillator with frequencies  $\omega_x = \omega_y = \omega_z = 2\pi 50$  Hz. The Fermi temperature for these parameters is  $T_F = 436$  nK.

Fermi Gas (DFG) is not a phase transition, and there is no absolute measure of the onset of degeneracy. Instead, a Fermi gas can be considered degenerate when the occupation function  $n(\epsilon)$  differs significantly from that of a thermal gas. This occurs when the temperature is of order  $0.2T_F$ .

### 2.2.2 Interactions and Feshbach resonances

Although the magnitude of the contact interaction  $U_0$  for DFGs is not intrinsically different from that of BECs. There are, however, two key differences. First, the Pauli exclusion principle forbids s-wave interactions between atoms of the same spin. Higher partial wave interactions are 'frozen out' at low temperatures, when the impact parameter of the collision becomes larger than the effective cross section of interactions (see [?], sec. 2.1.2). Therefore, in order to observe interactions, and indeed to cool the gas to degeneracy, another species needs to be present so that intraspecies s-wave interactions can occur. This can be a different atomic species or a different spin state of the same atom.

Second, the densities of standard DFGs ( $\approx 10^{12}$  atoms/cm<sup>3</sup>) are much lower than that of BECs ( $\approx 10^{14}$  atoms/cm<sup>3</sup>). Since the likelihood of two-body collisions is proportional to the atomic density  $\rho^2$ , this leads to a much smaller effect of interactions in DFGs.

A widely used technique for enhancing interaction effects in DFGs is Feshbach resonances. A Feshbach resonance occurs between two species (either atomic species or spin species of the same atom) when the open channel, ie the two particles independently in their external potential, energetically approaches a closed channel, ie a bound molecular state of the two species, shown schematically in Figure ??a.

Generally, the atoms in an open channel are energetically sensitive to a background magnetic field  $B$  via the hyperfine interaction  $H_B = \mu \cdot B$ , where  $\mu$  is the magnetic dipole moment. Tuning the magnetic field should therefore tune the energy of the open channel. The molecular bound state may also have an overall magnetic moment, but it is generally not identical to that of the two atoms in the open channel, and therefore varies differently with the background field. Figure ??b shows an example where the bound state has zero magnetic moment. Here, the energy of both the closed and open channel as a function of background magnetic field  $B$  is plotted in the vicinity of a Feshbach resonance. The resonance occurs at a field  $B_0$  where the energies of the two channels coincide.

Assuming there is at least infinitesimal coupling between the closed and open channels, as the energies of the two channels approach each other the perturbative correction term to the energy grows and the interaction between the atoms is effected. This is most easily seen in the s-wave case through changes the scattering length  $a$ . In the case where there are no inelastic two-body channels, such as for the <sup>40</sup>K resonance discussed in this thesis, the interatomic scattering length as a

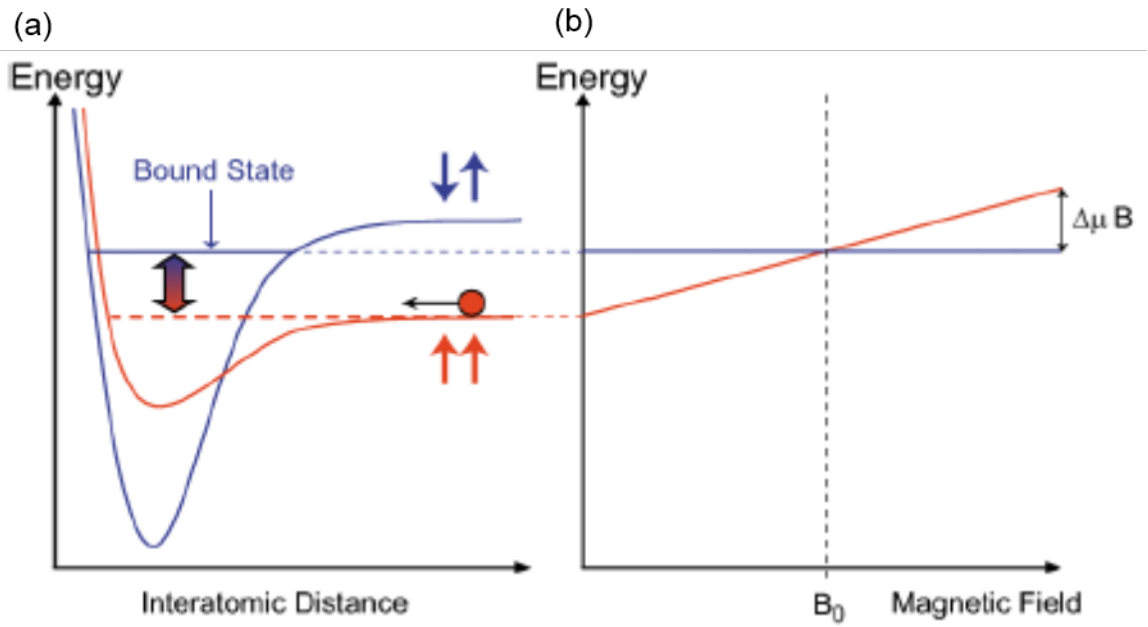


Figure 5: Schematic of a Feshbach resonance. (a) Pictorial representation of energy as a function of interatomic distance for an open channel (red) and closed channel (blue). (b) Energy as a function of background magnetic field  $B$  for the closed (blue) and open (red) channels. The energies coincide at the Feshbach resonance point  $B_0$ . Energy of Figure taken from [?].



function of background field is given by [?]

$$a(B) = a_{\text{bg}} \left( 1 - \frac{\Delta}{B - B_0} \right), \quad (2.26)$$

where  $a_{\text{bg}}$  is the background scattering length,  $\Delta$  is the width of the resonance, and  $B_0$  is the field value at which the resonance occurs. The scattering length diverges at the resonance.

The tunability of interactions provided by Feshbach resonances has allowed for creation of molecular Bose-Einstein condensates from Fermi gases [?, ?, ?] as well as observation of the phase transition from the Bardeen-Cooper-Schrieffer (BCS) superconducting regime to the BEC regime at sufficiently low temperatures [?, ?, ?, ?].

## 2.3 RbK apparatus

Bird's eye view picture

Brief description of BEC making procedure

Differences from Lauren's thesis:

Describe Hsin-I's new imaging path Describe extra lens for beam shaping the dipole trap

Brief description of DFG making procedure (of old)

Differences from Lauren's thesis: Describe 2D MOT'

## Chapter 3: Atom Light Interactions

### 3.1 Near-resonant atom-light interaction

In this section, we will assume the atom can be treated as a two-level system: one with a ground and excited atomic state, with an energy difference of energy difference  $\hbar\omega_0$ . When such an atom, starting in the ground state, is illuminated by a laser beam with frequency  $\hbar\omega_L$ , there are three kinds of transitions that occur: during absorption the atom absorbs a photon from the laser and goes from the ground to the excited state; during stimulated emission, the atom emits a photon into the field of the laser beam and jump from the excited to the ground state; during spontaneous emission, the atom decays to the ground state from the excited state with no help from the laser, emitting into a random vacuum mode. Stimulated emission results in coherent light co-propagating with the laser beam, while spontaneous emission results in light scattering incoherently in any direction. The rate of spontaneous emission from an excited state is given by the natural transition linewidth of the transition  $\Gamma$ .

On timescales short compared to  $1/\Gamma$ , spontaneous emission can be ignored, and an atom undergoes coherent Rabi oscillations between the ground and excited states via cycles of absorption and stimulated emission [5]. Taking  $c_g$  and  $c_e$  to be the time-dependent coefficients multiplying the eigenstate wavefunctions of the ground and excited state respectively, and assuming the atom starts in the ground

state  $c_g(t = 0) = 1$ , the excited state population is given by

$$c_e(t) = -i \frac{\Omega}{\Omega'} \sin\left(\frac{\Omega' t}{2}\right) e^{-i\delta t/2}, \quad (3.1)$$

where  $\Omega$  is the Rabi frequency given by  $\Omega^2 = \frac{\Gamma \lambda_L^3}{h(2\pi)^3} I$ , with  $\lambda_L$  as the laser wavelength,  $h$  as Plank's constant and  $I$  as the laser intensity,  $\Omega' = \sqrt{\Omega^2 + \delta^2}$  is the generalized Rabi frequency and  $\delta = \omega_0 - \omega_L$  is the detuning of the laser from atomic resonance.

In the regime where spontaneous emission cannot be ignored, Rabi oscillations of each individual atom are intermittently interrupted by decay to the ground state. Averaging over an atomic ensemble, on the time scale of a single Rabi oscillation the overall excited state population reaches a steady state, and the rate of spontaneous emission becomes constant. Since during spontaneous emission the ejected photon can go into any vacuum mode, this process can be thought of as the scattering of photons by the atoms. This scattering rate is given by [5]

$$\gamma_{\text{sc}} = \frac{\Gamma}{2} \frac{I/I_{\text{sat}}}{1 + 4(\delta/\Gamma)^2 + I/I_{\text{sat}}}, \quad (3.2)$$

where  $I_{\text{sat}}$  is the saturation intensity. This is the intensity at which the timescale of spontaneous emission matches the Rabi oscillation rate, reducing the capacity for absorption of extra light.

## 3.2 Absorption imaging

Absorption imaging takes advantage of the on-resonant interaction described in the previous section. An on or near-resonant laser beam ( $\delta/\Gamma \ll 1$ ) is shined at the atoms, and the absorbed light acts to create a shadow in the shape of the atoms in the laser beam. This beam with the shadow is then imaged on a camera, in our case a CCD, as depicted in Figure 1a (top). This is called the atom image,

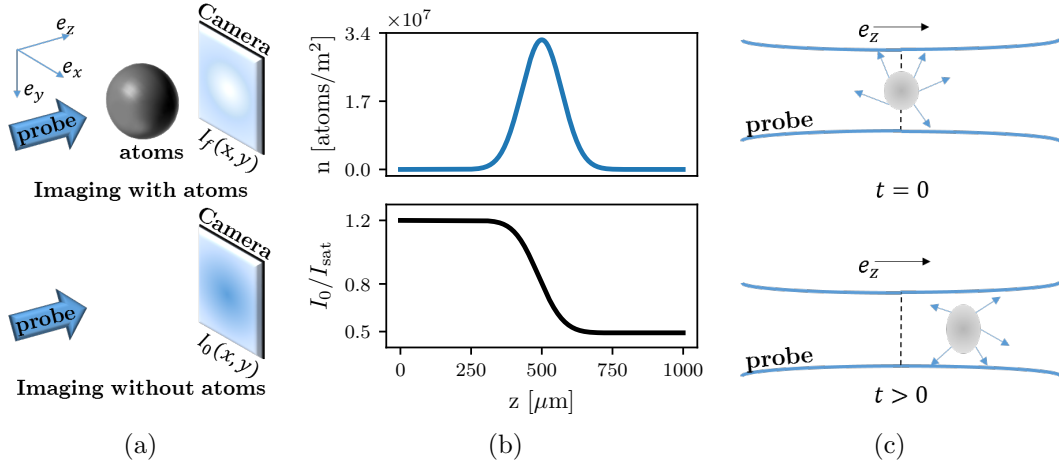


Figure 1: Absorption imaging. (a) Near resonant probe light illuminates the atoms, and the transmitted light (containing a shadow of the atoms) is imaged on the camera. A second image taken with no atoms provides a reference. (b) The probe beam is partially absorbed as it traverses the cloud, and the intensity seen by atoms further along the imaging direction  $e_z$  is lowered. (c) An atomic cloud illuminated by a probe light field absorbs photons from the probe and re-emits them in all directions. This process results in a net acceleration of the cloud in the direction of the probe light as well as diffusive spreading in the transverse directions.

and the intensity distribution over the camera is denoted by  $I_f(x, y)$ , where the subscript f stands for final - the intensity after the light has encountered the atoms. To quantify the 'shadowed out' intensity, after the atoms have left the trap the same laser intensity is shined directly at the camera, as in Figure 1a (bottom). This is called the probe image, and the intensity distribution over the camera is denoted by  $I_0(x, y)$ , where the subscript 0 indicated initial - the intensity before the light had encountered the atoms.

To recover the atom number distribution encountered by the light, consider an atomic cloud with 3D density  $\rho(x, y, z)$ . Since we can only obtain 2D information from the camera, we can only hope to recover a 2D atomic column density  $n(x, y) = \int \rho(x, y, z) dz$ . Focusing in on a single pixel of the camera, we can consider a single value of  $I_0$  and  $I_f$  to recover a local  $n$ . As the laser light propagates through the atomic cloud, the intensity of the light will diminish due to absorption. This

absorption as a function of propagation direction  $z$  can be expressed using the scattering rate equation Eq. 3.2 as the number of photons scattered by the atoms (proportional to the atomic density times the scattering rate) times the photon energy  $\hbar\omega_L$ :

$$\frac{d}{dz} \frac{I(z)}{I_{\text{sat}}} = -\hbar\omega_L \rho(z) \gamma_{sc}(z) = -\rho(z) \sigma_0 \frac{I(z)/I_{\text{sat}}}{1 + 4\delta^2/\Gamma^2 + I(z)/I_{\text{sat}}}, \quad (3.3)$$

where the resonant scattering cross section is  $\sigma_0 = 3\lambda_0^2/2\pi$ , and  $\lambda_0$  is the wavelength associated with atomic resonance.

Integrating both sides of Eq. 3.3, we obtain

$$\sigma_0 n = (1 + 4\delta^2/\Gamma^2) \ln(I_0/I_f) + (I_0 - I_f)/I_{\text{sat}}. \quad (3.4)$$

The quantity  $OD = \ln(I_0/I_f)$  is called the optical depth of the cloud. When the probe intensity  $I_0$  is much smaller than the saturation intensity, the second term in Eq. 3.4 becomes negligible. Assuming further that the probe light is on resonance,  $\delta = 0$ , the atomic column density becomes simply  $\sigma_0 n = OD$ . Figure 1b shows a Gaussian atomic density distribution (top) and the resulting probe intensity as a function of position in the cloud (bottom). The intensity drops from its initial to final value gradually as it traverses the cloud.

However, there is an important effect that the above equations do not account for. Namely, as the atoms absorb light from the probe beam, they also get a momentum kick equal to the momentum of a photon during each collision  $\hbar k_r = h/\lambda_L$  in the direction of propagation. It is true that the absorbed photon will then be re-emitted by the atom, inducing a loss of momentum, but since this happens through the process of spontaneous emission into a random vacuum mode, the average momentum kick acquired this way over many re-emissions will average to zero. On average, each photon absorbed will induce a change in velocity of the atom of  $v_r = \hbar k_r/m$ ,

where  $m$  is the atomic mass, as depicted in Fig. 1c. As the velocity of the atom changes, due to the Doppler effect, the apparent laser frequency will change as well. Therefore, even if the laser light is exactly on-resonant for a stationary atom, it will become off-resonant for longer imaging times, and Eq. 3.3 will acquire a time dependence. For most experiments, this effect is small and can be neglected. However, if the imaging time becomes of order a recoil time  $t_r$ , a time after which the recoil-induced detuning  $\delta$  becomes of order  $\Gamma$ , this effect becomes significant. We explore this effect in Chapter ??.

### 3.2.1 Time-of-flight and in situ imaging

There are two commonly used protocols for measuring cold atomic clouds, in situ and time of flight measurements. Generally, the atomic cloud is trapped (in our case by an optical dipole trap) during the experiment. In situ is Latin for in its original place. As suggested by the name, in situ measurements are taken while the cloud is still in its original trap, or immediately after the trap is turned off before any dynamics have had time to occur. These measurements measure the real spatial distribution of the atoms at the end of the given experiment. There is a difficulty associated with making in situ measurements of BECs, however. Namely, BECs in their original trap tend to be relatively dense, with optical depths often in excess of  $OD \approx 20$ , requiring unrealistic probe light intensities to resolve. One way to bypass this difficulty is to selectively image only a small fraction of the condensed atoms, as was done with microwave imaging for our magnetic field stabilization feedforward protocol [INSERT SECTION REFERENCE HERE ONCE ITS WRITTEN]. Another option is to instead perform a time-of-flight measurement.

In time-of-flight measurements, the trapping potential is abruptly snapped off after the experiment, and the atoms are allowed to free fall and expand for some time  $t$ . For our experiments,  $t$  was on the order of tens of milliseconds. In the

regime where time  $t$  is long enough that the atoms travel much further than the initial extent of the cloud in the directions transverse to the imaging axis, the final position of the atoms is determined almost exclusively by their in situ momentum, not their in situ position. Therefore, time-of-flight imaging in this regime measures the atomic distribution as a function of momentum, not position.

### 3.3 One dimensional optical lattices

#### 3.3.1 Far off-resonant atom-light interaction

As described in section 3.1, on timescales where spontaneous emission can be neglected, two-level atoms exposed to laser radiation undergo coherent Rabi oscillations between the two levels. Starting with  $c_g$  and  $c_e$  as the time-dependent coefficients multiplying the eigenstate wavefunctions of the ground and excited state respectively, and assuming the atom starts in the ground state  $c_g(t=0) = 1$ , we make the traditional transformation to the rotating frame:

$$c'_g(t) = c_g(t) \tag{3.5}$$

$$c'_e(t) = c_e(t)e^{-i\delta t}, \tag{3.6}$$

where  $\delta$  is the detuning of laser light from resonance. In this frame, we can write the atom-light Hamiltonian in the  $\begin{pmatrix} c'_g \\ c'_e \end{pmatrix}$  basis as:

$$H = \hbar \begin{pmatrix} -\delta/2 & \Omega/2 \\ \Omega/2 & \delta/2 \end{pmatrix}, \tag{3.7}$$

where  $\Omega$  is the coupling strength, also known as the Rabi frequency. In the limit of no coupling,  $\Omega = 0$ , in the rotating frame the eigenenergies are  $E_{\pm} = \pm\hbar\delta/2$ .

For non-zero coupling, finding the eigenvalues of  $H$  gives  $E_{\pm} = \pm\hbar\sqrt{\delta^2 + \Omega^2}/2$ . Therefore, the bare (without light) eigenenergies are shifted in the presence of the light.

For a far detuned laser beam, one expects that no absorption of the light will actually take place, and the atom will remain entirely in the ground state. Indeed, solving the Shroedinger equation with the above Hamiltonian

$$i\hbar\frac{d}{dt}\begin{pmatrix} c'_g \\ c'_e \end{pmatrix} = H \begin{pmatrix} c'_g \\ c'_e \end{pmatrix} \quad (3.8)$$

we obtain the oscillating excited state population

$$c'_e(t) = -i\frac{\Omega}{\sqrt{\Omega^2 + \delta^2}}\sin\left(\frac{\sqrt{\Omega^2 + \delta^2}t}{2}\right), \quad (3.9)$$

where the amplitude of the oscillation approaches zero in the limit  $\Omega \ll \delta$ . Thus, the only effect of the light in this regime is to shift the eigenenergies of the ground and excited states. Expanding the energies in the small parameter  $\Omega/\delta$ , we obtain the shifted energies  $E_{\pm} = \pm\hbar\sqrt{\delta^2 + \Omega^2}/2 \approx \pm(\delta/2 + \Omega^2/4\delta)$ . The shift from bare energy levels is thus

$$\Delta E_{\pm} = \pm\Omega^2/4\delta. \quad (3.10)$$

This laser intensity dependent energy shift is called the AC Stark shift, and is the basis of most laser created potentials for cold atoms.

For the ground state, and a red detuned laser beam (where the laser frequency is lower than the resonant frequency), this creates energy minima in locations of maximal laser intensity. For the lattice described in this chapter, as well as for the trapping of our atoms in the final stages of cooling, we use high power (up to 10 W) lasers with wavelength  $\lambda_L = 1064$  nm.



### 3.3.2 Lattice Hamiltonian

Our 1-D optical lattice is created by retro-reflecting the  $\lambda_L = 1064$  nm laser, creating a standing wave of light. Via the AC Stark shift, this creates a periodic potential for the atoms of the form

$$V = V_0 \sin^2(k_L x), \quad (3.11)$$

where  $k_L = 2\pi/\lambda_L$  is the wavenumber associated with the lattice recoil momentum. The time-independent Hamiltonian, for some eigenenergy  $E_n$ , will be given by

$$-\frac{\hbar^2}{2m} \frac{d^2}{dx^2} \Psi_n(x) + V_0 \sin^2(k_L x) \Psi_n(x) = E_n \Psi_n(x). \quad (3.12)$$

Since the potential is spatially periodic, we can invoke Bloch's theorem [6]:

$$\Psi_{n,q} = e^{iqx} u_{n,q}(x), \quad (3.13)$$

where  $q$  is the crystal momentum restricted to  $\pm \hbar k_L$ , and  $u_{n,q}(x)$  is the spatially varying part of the wavefunction. Plugging this in to the Hamiltonian, we obtain

$$-\frac{\hbar^2}{2m} \left( -q^2 + 2iq \frac{d}{dx} + \frac{d^2}{dx^2} \right) u_{n,q}(x) + V_0 \sin^2(k_L x) u_{n,q}(x) = E_n u_{n,q}(x). \quad (3.14)$$

Expanding  $u_{n,q}(x)$  in Fourier components commensurate with the lattice period of  $2k_L$  as  $u_{n,q}(x) = \sum_{j=-\infty}^{\infty} a_j e^{i2k_L j x}$ , we obtain

$$\sum_j \left( \frac{\hbar^2}{2m} (q + 2k_L)^2 a_j + V_0 \sin^2(k_L x) a_j \right) e^{i2k_L j x} = E_n \sum_j a_j e^{i2k_L j x}. \quad (3.15)$$

Re-writing  $\sin^2(k_L x) = (e^{-2ik_L x} + e^{2ik_L x} - 2)/4$ , multiplying both sides by  $e^{i2k_L j' x}$  and invoking  $\sum_j c_j e^{ik(j-j')} = \delta_{jj'}$ , where  $\delta_{jj'}$  is the Kroniker delta and  $c_j$  are appropriately

normalized coefficients, we get for any value of the index  $j$

$$\frac{\hbar^2}{2m}(q + 2k_L j)^2 a_j - \frac{V_0}{4}(a_{j+1} + a_{j-1}) = E_n a_j. \quad (3.16)$$

This can be expressed in matrix form

$$H_L = \begin{pmatrix} \ddots & & & & & \\ & \frac{\hbar^2}{2m}(q + 4k_L)^2 & \frac{V_0}{4} & 0 & 0 & 0 \\ & \frac{V_0}{4} & \frac{\hbar^2}{2m}(q + 2k_L)^2 & \frac{V_0}{4} & 0 & 0 \\ & 0 & \frac{V_0}{4} & \frac{\hbar^2}{2m}q^2 & \frac{V_0}{4} & 0 \\ & 0 & 0 & \frac{V_0}{4} & \frac{\hbar^2}{2m}(q - 2k_L)^2 & \frac{V_0}{4} \\ & & 0 & 0 & \frac{V_0}{4} & \frac{\hbar^2}{2m}(q - 4k_L)^2 \\ & & & & & \ddots \end{pmatrix}, \quad (3.17)$$

in the basis of momentum orders  $|k\rangle = e^{ikx}$  given by:

$$\begin{pmatrix} \vdots \\ |q + 4k_L\rangle \\ |q + 2k_L\rangle \\ |q\rangle \\ |q - 2k_L\rangle \\ |q - 4k_L\rangle \\ \vdots \end{pmatrix}. \quad (3.18)$$

This matrix can be diagonalized for every value of the crystal momentum  $q$ , with the resulting band structure shown in Figure 2. It is convenient to define the lattice recoil energy  $E_L = \hbar^2 k_L^2 / 2m$ . Then, we can re-write the Hamiltonian with

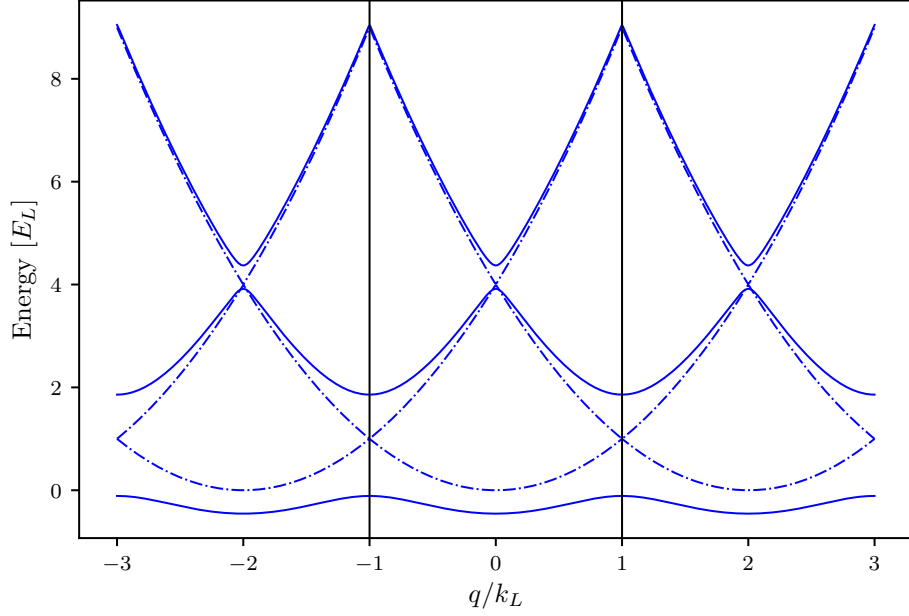


Figure 2: Lattice band structure in the extended zone scheme. The dashed lines represent the limit of zero lattice depth, with the regular parabolic dispersion relation of a free particle repeating with reciprocal lattice period. The solid lines are the dispersion relation at  $V_0 = 4.0 E_L$ , showing the opening of gaps at crossings of the zero lattice depth bands. The black lines demarcate the first Brillouin zone.

$V_0$  in units of  $E_L$  and momenta  $q$  in units of  $k_L$  as

$$H_L/E_L = \begin{pmatrix} \ddots & & & & & \\ & (q+4)^2 & \frac{V_0}{4} & 0 & 0 & 0 \\ & \frac{V_0}{4} & (q+2)^2 & \frac{V_0}{4} & 0 & 0 \\ & 0 & \frac{V_0}{4} & q^2 & \frac{V_0}{4} & 0 \\ & 0 & 0 & \frac{V_0}{4} & (q-2)^2 & \frac{V_0}{4} \\ & & 0 & 0 & \frac{V_0}{4} & (q-4)^2 \\ & & & & & \ddots \end{pmatrix}. \quad (3.19)$$

In any numerical simulation, the number of momentum orders that can be included is finite. We determine the value of the parameter  $n = \max(|j|)$  as the

lowest  $n$  at which the eigenvalues stop changing to machine precision from  $n - 1$ . The code for finding and plotting the eigenvalues and eigenvectors of the lattice hamiltonian is included in Appendix [MAKE APPENDIX WITH CODE?].

### 3.3.3 Tight binding approximation

In the limit of large lattice depths,  $V_0 > \approx 5E_L$ , the lattice Hamiltonian is well approximated by the tight-binding model. In the tight binding model, the basis is assumed to be a set of orthogonal functions, called Wannier functions, localized to each lattice site  $|j\rangle$ . The approximation lies in assuming only nearest neighbor tunnelings between the sites, forming the tight-binding Hamiltonian

$$H_{\text{tb}} = -t |j\rangle \langle j+1| + \text{H.c.}, \quad (3.20)$$

where  $t$  is the tunneling amplitude between nearest neighbor sites and H.c. stands for Hermitian conjugate. We have neglected the diagonal kinetic energy term, as it will be equal for every Wannier function  $|j\rangle$  and thus represents a constant energy offset. All the information about the lattice depth is therefore reflected in the tunneling amplitude  $t$ .

The tight binding Hamiltonian can also be expressed in the momentum basis by Fourier transforming the basis functions:

$$|j\rangle = \frac{1}{\sqrt{N}} \sum_{k_j} e^{-ik_j j} |k_j\rangle, \quad (3.21)$$

giving the Hamiltonian

$$H_{\text{tb}} = -\frac{1}{N} \sum_{k_1} \sum_{k_2} k_2 t e^{-ik_1} e^{ik_2(j+1)} |k_1\rangle \langle k_2| + \text{H.c} = 2t \cos(k) |k\rangle \langle k|. \quad (3.22)$$

From this we can directly read off the band structure of the tight binding Hamilto-

nian. First, we notice that we only obtain one band - to approximate higher bands with the tight binding approximation we would need to construct a different set of Wannier functions and a different tunneling strength. Second, we see that the lowest band is simply a cosine - therefore we have solved for the band structure without even defining what the basis Wannier functions are! Third, the amplitude of the cosine function is given by the tunneling strength  $t$ . This gives us a good clue as to how to determine the appropriate tunneling given a lattice depth  $V_0$  - simply find a  $t$  that matches the amplitude of the lowest band, which becomes cosinusoidal in the deep lattice limit.

The precise form of the Wannier functions depends on both the depth of the lattice and the band being reproduced. It is not necessary for us to find their full expression, as the band structure can be calculated without them. The definition, however, is

$$|j\rangle = \int_{\text{BZ}} e^{i\phi(q)-iqja} \Psi_q(x) dq, \quad (3.23)$$

where the integral is over the Brillouin zone, from  $-k_L$  to  $k_L$ ,  $a$  is the lattice spacing  $\lambda_L/2$ , and  $\Psi_q$  is the Bloch wavefunction at crystal momentum  $q$ , and  $\phi(q)$  is the phase associated with each Bloch wavefunction. The Bloch wavefunctions individually have arbitrary phase. The phase plays an important role in combining the Bloch wavefunctions into a Wannier function, finding the proper phase relationship to make the wavefunction maximally localized at each site [7].

### 3.3.4 Pulsing vs adiabatic loading of the lattice

The lattice depth parameter  $V_0/4$ , for a range of values, can be well calibrated experimentally by pulsing on the lattice. Here, the word pulsing indicates that the lattice is turned on fully non-adiabatically, if not instantaneously, such that the original bare momentum state is projected onto the lattice eigenbasis, as shown

in Figure 5a. If the atoms start out stationary in the trap, the bare state in the momentum basis is simply

$$|\Psi_0\rangle = \begin{pmatrix} \vdots \\ 0 \\ 0 \\ 1 \\ 0 \\ 0 \\ \vdots \end{pmatrix}, \quad (3.24)$$

as depicted in Figure 5b.

Since the lattice eigenbasis is distinct from the bare one, instantaneously turning on the lattice will necessarily excite the atoms into a superposition of lattice eigenstates, each evolving with a different phase according to the eigenenergy while the lattice is on, as shown in Figure 5c. Then, when the lattice is snapped back off, the wavefunction is projected back into the bare basis, and the varying phase accumulation results in a beating of the different momentum orders, see Figure 5d. This can be calculated simply by using the time evolution operator

$$|\Psi(t)\rangle = e^{-iH_L t/\hbar} |\Psi_0\rangle. \quad (3.25)$$

By pulsing on the lattice for variable amounts of time  $t$ , we can obtain fractional populations in the different momentum states. Time-of-flight imaging captures the momentum distribution of the cloud, and the different entries of  $\Psi(t)$  in the momentum basis will thus appear as different clouds on the absorption image, as shown in Figure 4a. The fractional population in these clouds corresponds to a measurement of  $|a_j|^2$ . Typically for our values of the lattice depth  $V_0 < 10E_L$ , it is sufficient to simply count three central momentum orders,  $k = q, q \pm 2k_L$ . Then, we can fit Eq.

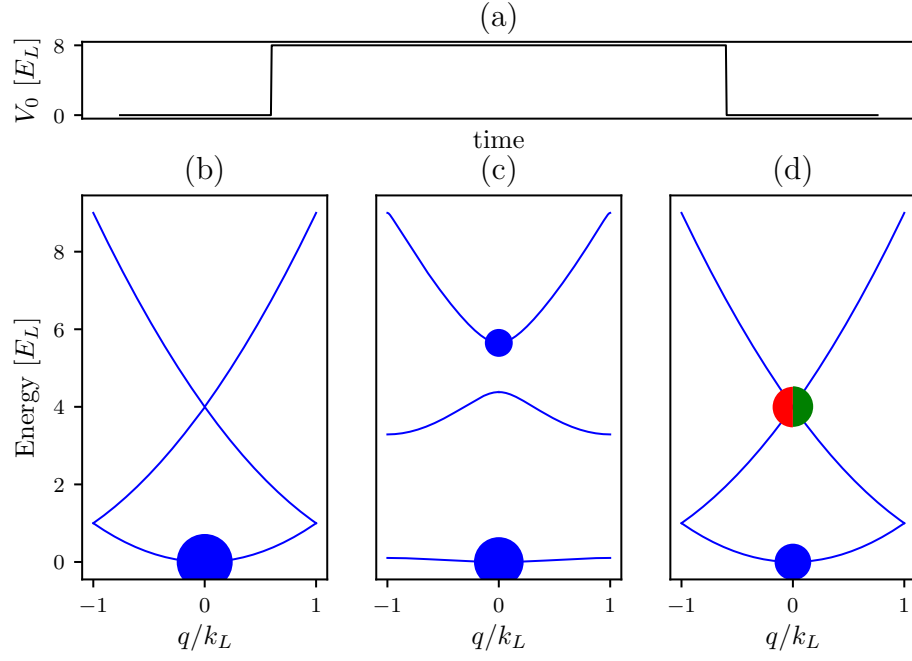


Figure 3: Lattice pulsing. (a) Lattice depth as a function of time during a pulsing experiment. The lattice is turned on instantaneously at  $t = 0$  and held on for a variable amount of time until being turned off instantaneously at a final time  $t = t_f$ . (b) Atomic population before  $t = 0$ . The dispersion relation is that of a free particle, and all of the atoms start out at  $q = 0$  in the lowest energy level. Here, the area of the dots is proportional to the fractional population in the energy state. (c) Atomic population after the lattice is turned on for a lattice depth of  $V_0 = 8.0E_L$ . The energy spectrum now shows the lattice band structure, and some atomic population is projected onto the excited bands. (d) Atomic population after the lattice is snapped off at  $t_f = 150 \mu\text{s}$ . The wavefunction is projected back onto the bare states, with some fraction (blue circle) in the lowest band at  $k = 0$  and some fraction in the excited band, with equal population being projected onto the  $k = 2k_L$  (green) and  $k = -2k_L$  (red).

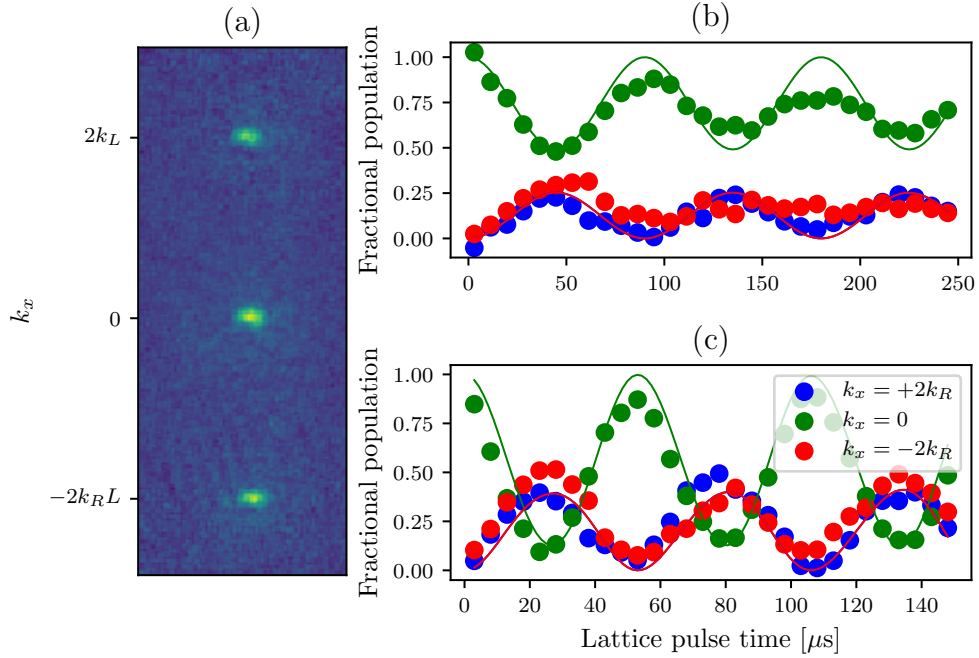


Figure 4: Lattice pulsing for calibration. (a) An example time-of-flight image from a pulsing experiment. The three different clouds are different momentum orders. (b) Fractional populations in the different momentum orders as a function of pulsing time at a low lattice power. Data is indicated by dots and best fit theory is represented by lines. The lattice depth from fit is  $V_0 = 5.57 \pm 0.07 E_L$ . (c) Fractional populations in the different momentum orders as a function of pulsing time at a higher lattice power. Data is indicated by dots and best fit theory is represented by lines. The lattice depth from fit is  $V_0 = 12.69 \pm 0.07 E_L$ .

3.25 to the data with fitting parameter  $V_0$ , thus deducing the lattice depth. Some examples of these pulsing experiments are presented in figure 4b,c.

In contrast to pulsing, adiabatic loading turns the lattice on slowly, such that the atomic wavefunction starting in the bare ground state can continuously adjust to remain in the ground state of the current Hamiltonian, without projecting onto any of the higher bands. This process is illustrated in Figure 5. The adiabatic timescale depends on the spacing between the ground and next excited band (or if starting in a different eigenstate, the nearest eigenstate). If the energy difference between the ground and first excited state is  $\Delta E$ , the timescale on which the lattice



is turned on must fulfill  $t \gg \hbar/\Delta E$ .

### 3.4 Raman and rf coupling

#### 3.4.1 Hyperfine structure

Alkali atoms' energy levels can be understood as primarily the energy state of the single electron in the outer shell. Fine structure arises from different combinations of angular momenta, including orbital angular momentum of the outermost electron with respect to the nucleus  $\mathbf{L}$ , the electron spin  $\mathbf{S}$  and the nuclear spin  $\mathbf{I}$ . The total electron angular momentum is the combination of orbital and the spin angular momenta  $\mathbf{J} = \mathbf{L} + \mathbf{S}$ , and the quantum number can be any integer  $|L - S| \leq J \leq |L + S|$ . The ground state of  $^{87}\text{Rb}$ , in term notation  $^{2S+1}L_J$  is  $^2S_{1/2}$ , where  $S$  is orbital notation indicating  $L = 0$ . Since the total spin quantum number  $J = 1/2$ , this produces two possible spin projection quantum numbers,  $m_J = \pm 1/2$ .

There is also a contribution from the nuclear spin  $\mathbf{I}$ , resolvable at low magnetic fields, which gives rise to hyperfine structure of the states. For  $^{87}\text{Rb}$ ,  $I = 3/2$ . The total spin, including nuclear spin, is indicated by the quantum number  $F$ , and  $|J - I| \leq F \leq |J + I|$ . The interaction with the nuclear spin splits the ground state of  $^{87}\text{Rb}$  into two manifolds,  $F = 1$  and  $F = 2$ , with three hyperfine states in the  $F = 1$  manifold ( $m_F = 0, \pm 1$ ) and five hyperfine states in the  $F = 2$  manifold ( $m_F = 0, \pm 1, \pm 2$ ). These states couple to an external magnetic field  $B_z$  along some direction  $\mathbf{e}_z$  via the Hamiltonian  $H_B = \mu_B(g_J J_z + g_I I_z)B_z/\hbar$ . Here  $\mu_B$  is the Bohr magneton, and  $g_J$  and  $g_I$  are Lande g-factors. Since  $g_J \gg g_I$ , at high fields the nuclear spin interaction becomes small compared to the total energy shift, and the levels are grouped according to their  $m_J$  quantum number, as seen in Figure 6.

At low fields, however, the states are approximately linearly dependent on the  $m_F$  quantum number. The linear shift from the  $B = 0$  states is known as the linear

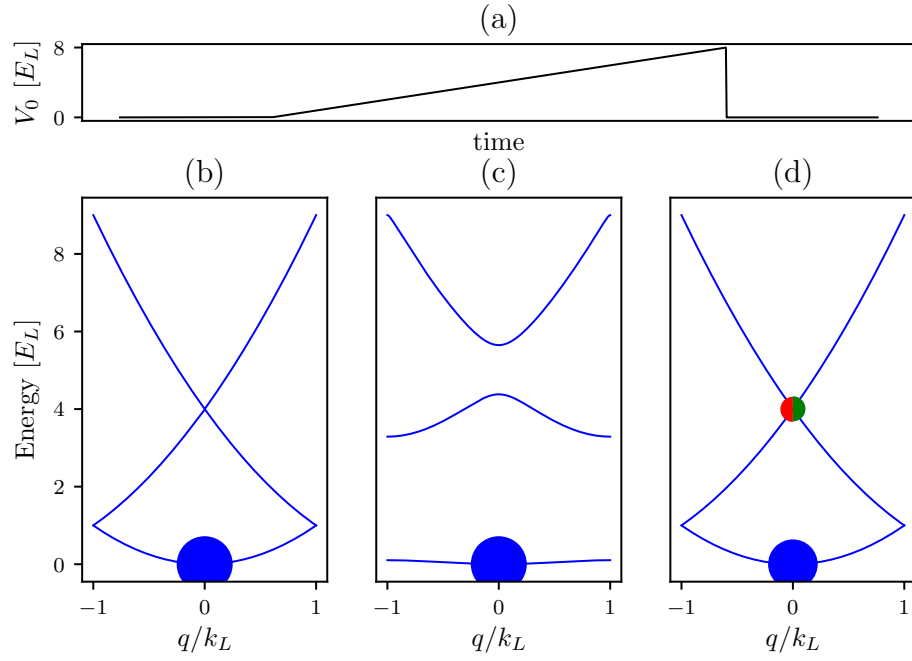


Figure 5: Adiabatic lattice loading. (a) Lattice depth as a function of time during adiabatic turn-on. The lattice is ramped on starting at  $t = 0$ , slowly increasing to a final lattice depth and turned off instantaneously at a final time  $t = t_f$ . (b) Atomic population before  $t = 0$ . All atoms are at  $k = 0$  in the lowest bare band. (c) Atomic population after the lattice is turned on adiabatically to a lattice depth of  $V_0 = 8.0E_L$ . All atoms remain in the lowest band, but the band is no longer bare. (d) Atomic population after the lattice is snapped off. The wavefunction is projected back onto the bare states, with some fraction (blue circle) in the lowest band at  $k = 0$  and some fraction in the excited band, with equal population being projected onto the  $k = 2k_L$  (green) and  $k = -2k_L$  (red). Since the lowest lattice band is a superposition of bare bands, some atoms are excited to the higher bare bands.

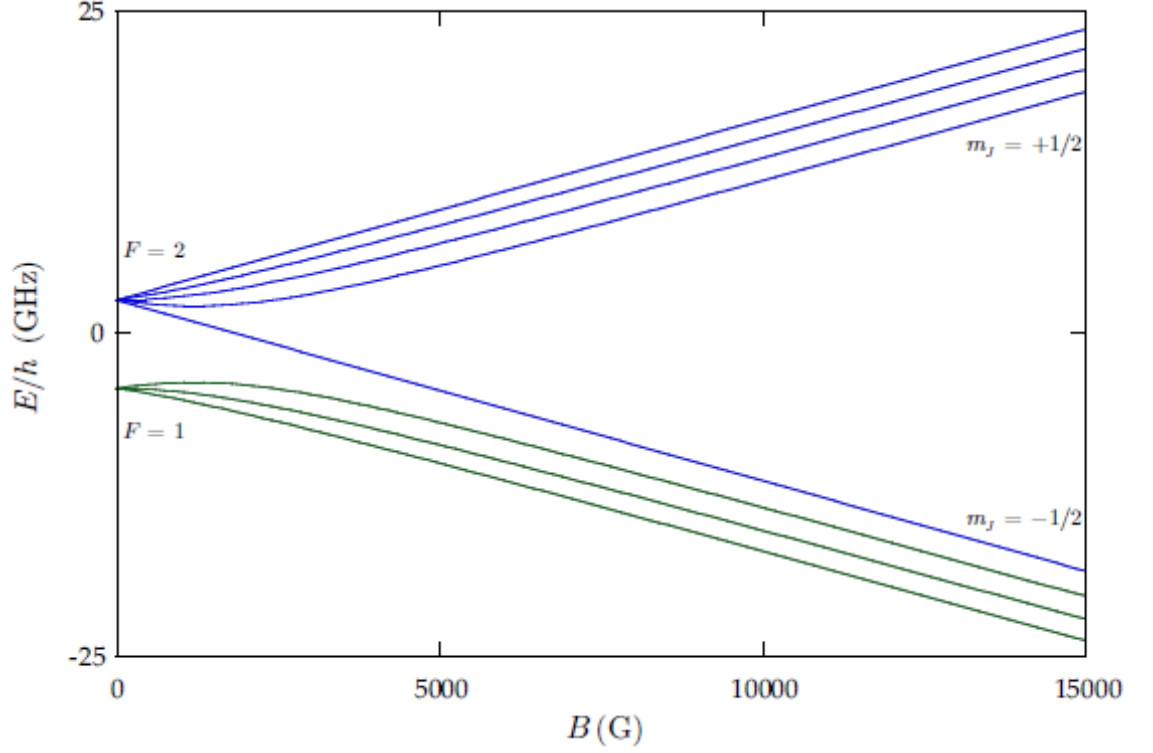


Figure 6: Energy structure of hyperfine states of the ground state of  $^{87}\text{Rb}$  as a function of external magnetic field strength in Gauss. Figure from ref. [1]

Zeeman shift. In the intermediate regime, the correction to the linear shift can be expressed in terms of an energy correction to each hyperfine state  $\epsilon(B)|m_F|^2$ , known as the quadratic Zeeman shift. For the magnetic fields used in experiments described in this thesis, this correction is sufficient for describing the energy levels.

The form of the Hamiltonian in this regime for any value of  $F$  is given by

$$H_0 = H_{\text{KE}} + \hbar\omega_z \mathbf{F}_z + \hbar\epsilon \mathbf{F}_z^2, \quad (3.26)$$

where  $\hbar\omega_z = \mu_B g_F B_z / \hbar$ , and the kinetic energy Hamiltonian  $H_{\text{KE}} = \hbar^2 \vec{k}^2 / 2m\mathcal{I}$ , and  $\mathcal{I}$  is the identity matrix.

### 3.4.2 Rf coupling Hamiltonian

For the  $F = 1$  manifold, there are three available spin states  $m_F = 0, \pm 1$ . There are many ways of introducing coupling terms between the different hyperfine states. Here, we will explain two methods: rf coupling and Raman coupling. Rf coupling is a radio-frequency oscillating magnetic field, in our case produced by a pair of circular coils in series side by side above the atoms (see [8]). Assuming the rf oscillating field is polarized along the  $\mathbf{e}_x$ , with the bias field along  $\mathbf{e}_z$ , the coupling Hamiltonian is given by  $H_{rf} = \mu_B g_F \vec{\mathbf{F}} \cdot \vec{\mathbf{B}} = \mu_B g_F \mathbf{F}_x B_x \cos(\omega t)$ , where  $2\pi\omega$  is the rf frequency. The schematic of this setup is shown in Figure 7. The eigenstates of the bare Hamiltonian  $H_0$  are the constituent  $m_F$  states. The eigenstates of the coupled Hamiltonian  $H_0 + H_{rf}(t)$  can be expressed as a linear superposition of the bare eigenstates  $\Psi(\vec{x}, t) = \sum_{m_F} c_{m_F}(t) \phi_{m_F}(\vec{x}) e^{-i\omega_{m_F} t}$ . The Hamiltonian in this basis can then be written as [5]

$$H_{\text{rf}} = H_{\text{KE}} + \hbar \begin{pmatrix} 0 & \Omega \cos(\omega t) e^{i\omega_z t} & 0 \\ \Omega \cos(\omega t) e^{-i\omega_z t} & 0 & \Omega \cos(\omega t) e^{i\omega_z t} \\ 0 & \Omega \cos(\omega t) e^{-i\omega_z t} & 0 \end{pmatrix}, \quad (3.27)$$

where  $\Omega$  is the Rabi frequency, proportional to  $B_x$ . We can then transfer into the rotating frame  $c'_{m_F} = e^{-im_F \delta t} c_{m_F}$ , where  $\delta = \omega_z - \omega$ . Then we apply the rotating wave approximation, that the fast oscillating terms average to zero over time scales of interest  $e^{2i\omega t} \approx 0$ , and obtain

$$H_{\text{rf}} = H_{\text{KE}} + \hbar \begin{pmatrix} \delta & \Omega/2 & 0 \\ \Omega/2 & -\epsilon & \Omega/2 \\ 0 & \Omega/2 & -\delta \end{pmatrix}, \quad (3.28)$$

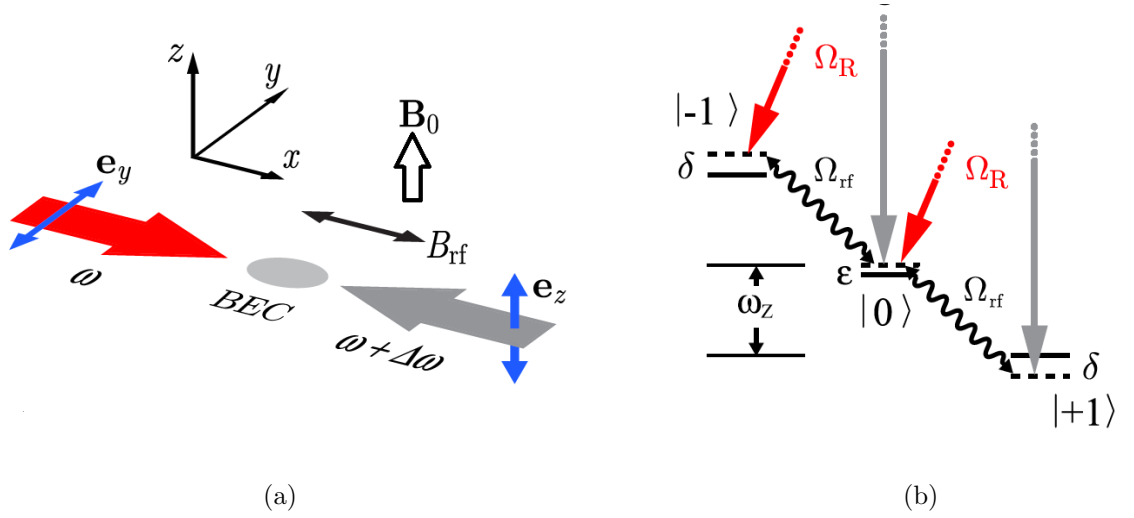


Figure 7: Raman and rf coupling schematic. (a) Beam geometry of the Raman beams and rf relative to the external field. The Raman beams have a frequency difference  $\Delta\omega$ , and are linearly polarized in perpendicular directions. (b) Level structure of both Raman and Rf coupling for hyperfine states of the  $F = 1$  manifold. The hyperfine splitting separates the levels by an energy  $\hbar\omega_z$ . The quadratic Zeeman shift  $\epsilon$  lowers the energy of the  $m_F = 0$  state, and the detuning  $\delta$  of either the Raman or the rf fields shifts the energies of the  $m_F = \pm 1$  states. Raman transitions are two-photon, exciting up to a virtual state and coming back down to an adjacent hyperfine state, with an accompanying momentum transfer. Rf couples adjacent hyperfine states directly. Figure taken from ref. [2]

or for any value of  $F$

$$H_{\text{rf}} = H_{\text{KE}} + \hbar\delta F_z + \hbar\epsilon F_z^2 + \Omega F_x/2. \quad (3.29)$$

The band structure of this Hamiltonian can be seen in Figure 8, where we have diagonalized Eq. 3.28 for a range of momenta  $k_x$  (we have isolated  $k_x$  for comparison with Raman coupling, as will be seen in the next section). The parabolas are simply the free particle dispersion relations along one dimension, with three bands arising from the three available spin states. It is convenient to define the magnetization of an eigenstate  $m = \sum_{m_F} m_F * p_{m_F}$ , where  $p_{m_F}$  is the fractional population in the  $m_F$  state. We have indicated the magnetization of the eigentate by coloring the

eigenenergies, with  $m = -1$  in red,  $m = 0$  in green, and  $m = +1$  in blue. In Figure 8a, both the detuning and the coupling strength are zero. Therefore, there are simply three free particle dispersions, each exactly correlated with a particular spin state, the  $m_F = \pm 1$  are degenerate and the  $m_F = 0$  state is slightly offset by the quadratic shift  $\hbar\epsilon$ . In Figure 8c, the coupling strength is again zero, but the detuning has been turned on, lifting the degeneracy between the  $m_F = \pm 1$  states. Figure 8b,d shows the same conditions as a,c, respectively, but with the coupling strength turned on. In Figure 8b, where the detuning is zero and the quadratic shift is negligible compared to the coupling strength, all states average to a magnetization of zero—the  $m_F = \pm 1$  states are symmetrically populated. In Figure 8d, this symmetry is broken by the presence of a detuning.

### 3.4.3 Raman coupling Hamiltonian

The counter-propagating Raman beams, as seen in Figure 7, couple the same states as the rf. They do so via the vector light shift created by the pair of beams. The electric field due to the right going beam (red in Figure 7a) is  $\mathbf{E} = E_0 \exp(ik_R x - i\omega t) \mathbf{e}_y$ , where  $E_0$  is the amplitude of the electric field and  $\hbar k_R = h/\lambda_R = \hbar\omega/c$ . The electric field from the left going beam (gray in Figure 7b) is  $\mathbf{E} = E_0 \exp(-ik_R x - i(\omega + \Delta\omega)t) \mathbf{e}_z$ . This combines to give an effective field from the vector light shift [9]  $B_{\text{eff}} \propto \mathbf{E} \times \mathbf{E}^* \propto -E_0^2 \cos(2k_R x + \Delta\omega t) \mathbf{e}_x$ . Going through the same procedure as for the rf coupling case, including the transfer into the rotating frame and the rotating wave approximation, we obtain the same Hamiltonian in the basis of bare spin states  $| -1 \rangle, | 0 \rangle, | 1 \rangle$  but with an extra phase factor:

$$H_{\text{Raman}} = H_{\text{KE}} + \hbar \begin{pmatrix} \delta & \Omega/2 e^{-i2k_R x} & 0 \\ \Omega/2 e^{i2k_R x} & -\epsilon & \Omega/2 e^{-i2k_R x} \\ 0 & \Omega/2 e^{i2k_R x} & -\delta \end{pmatrix}, \quad (3.30)$$

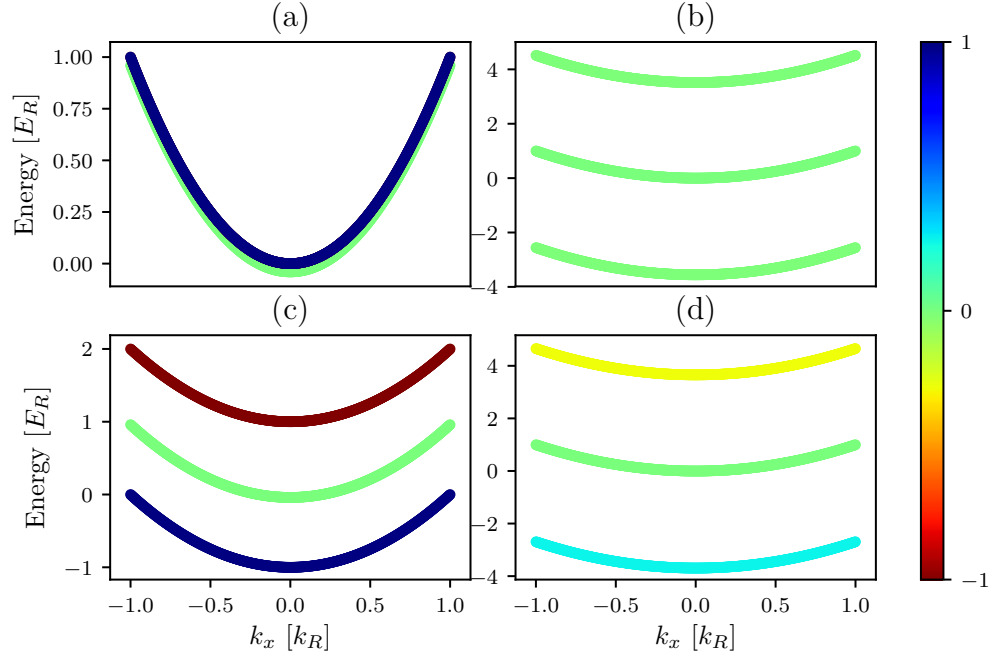


Figure 8: Band structure of the rf Hamiltonian, Eq. 3.28, in momentum space. For all plots, the quadratic Zeeman shift  $\hbar\epsilon = 0.04E_R$ , and the color represents magnetization, labeled by the colorbar. (a)  $\hbar\Omega = 0$ ,  $\hbar\delta = 0$ . No coupling or detuning is present, so the only separation between the bands is due to the quadratic shift  $\hbar\epsilon$ . (b)  $\hbar\Omega = 5.0E_R$ ,  $\hbar\delta = 0$ . (c)  $\hbar\Omega = 0$ ,  $\hbar\delta = 1.0E_R$ . Even though the coupling strength is zero, the bands are separated by the detuning. (d)  $\hbar\Omega = 5.0E_R$ ,  $\hbar\delta = 1.0E_R$ .

where  $\delta = \omega_z - \Delta\omega$ .

This phase difference between the rf and Raman Hamiltonian has an intuitive physical explanation. In order to undergo a Raman transition, an atom first absorbs a photon from one beam, getting a momentum kick equal to the recoil momentum  $\hbar k_R$ . Then, to decay back down to an adjacent spin state, the undergoes stimulated emission into the field of the other (counter-propagating) beam, acquiring another recoil momentum kick in the same direction for a total of  $2\hbar k_R \mathbf{e}_x$ . Therefore, the Raman coupling Hamiltonian for  $F = 1$ , after transforming into the rotating frame and performing the rotating wave approximation, can be written in the same way as the rf Hamiltonian in Eq. 3.28 with the addition of a momentum kick—in real space, an aquired phase—of  $e^{i2k_R x}$ .

We can again make a basis transformation to get rid of this phase. Let us define  $|-1\rangle' = \exp(-2ik_R x) |-1\rangle = |k_x - 2k_R, -1\rangle$ ,  $|0\rangle' = |0\rangle = |k_x, 0\rangle$ ,  $|1\rangle' = \exp(2ik_R x) |1\rangle = |k_x + 2k_R, 1\rangle$ , where for third definition we went into the momentum basis and labelled the states by a combination of their momentum and spin state. Then, including the kinetic energy term along  $\mathbf{e}_x$  explicitly, we obtain the Hamiltonian in the new basis as:

$$H_{\text{Raman}} = H_{\text{KE}}^{(y,z)} + \begin{pmatrix} \frac{\hbar^2(k_x - 2k_R)^2}{2m} + \hbar\delta & \hbar\Omega/2 & 0 \\ \hbar\Omega/2 & \frac{\hbar^2 k_x^2}{2m} - \hbar\epsilon & \hbar\Omega/2 \\ 0 & \hbar\Omega/2 & \frac{\hbar^2(k_x + 2k_R)^2}{2m} - \hbar\delta \end{pmatrix}. \quad (3.31)$$

It is convenient to define the Raman recoil energy as  $E_R = \frac{\hbar^2 k_R^2}{2m}$ . The band structure of this Hamiltonian is shown in Figure 9, for several representative parameter values, with the magnetization labelled by the color. Figure 9a shows the band structure in the limit of zero coupling and zero detuning, but where we have already gone into the basis  $|k_x - 2k_R, -1\rangle, |k_x, 0\rangle, |k_x + 2k_R, 1\rangle$ ; therefore, the free particle parabola corresponding to the  $m_F = 1$  spin states is shifted to center on



$k_x = -2k_R$  and the  $m_F = -1$  parabola is shifted to center on  $k_x = 2k_R$ . As the coupling is turned on to  $\hbar\Omega = 1E_R$  in Figure 9b, the points where the parabolas cross become 'avoided crossings', separating into three bands where magnetization (and the underlying spin distribution) depends on the momentum  $k_x$ . As the coupling strength is turned up even further to  $\hbar\Omega = 5E_R$  in Figure 9c, the lowest band goes from having three minima, one corresponding to each original spin state, to only one minimum. This transition happens at  $\hbar\Omega = 4E_R$  [8]. In Figure 9d, we show the band structure again in the limit of zero coupling, but this time with a detuning of  $\hbar\delta = 1.0E_R$ . Note that the detuning tips the parabolas with respect to each other. Figure 9e shows the detuned system with coupling strength turned up to  $\hbar\Omega = 1E_R$ , still in the three minima regime but with avoided crossings creating three momentum and spin coupled bands. In Figure 9f, the detuned system is turned up to a coupling strength of  $\hbar\Omega = 5E_R$ , creating a single minimum, this time offset from  $k_x = 0$ .

We can write the general  $F$  version of the Raman coupled Hamiltonian in the basis  $|k_x + m_F * 2k_R, m_F\rangle$ , where  $-F \leq m_F \leq F$ , as:

$$H_{\text{Raman}} = H_{\text{KE}}^{(y,z)} + \hbar^2(k_x\mathcal{I} + 2k_R F_z)^2/2m + \hbar\delta F_z + \hbar\epsilon F_z^2 + \Omega F_x/2. \quad (3.32)$$

### 3.4.4 Calibration of Raman and Rf dressed states

To calibrate the rf and Raman coupling strengths, we take a similar approach to the 1-D lattice calibration: start in a pure spin state, for example  $m_F = 0$ , and turn the coupling on non-adiabatically to induce Rabi oscillations between the coupled states. Then, during time-of-flight, apply a Stern-Gerlach gradient pulse to separate the spin components and observe the fractional populations in different spin states as a function of Rabi oscillation time.

Figure 10a,b shows example images obtained in time-of-flight when pulsing on

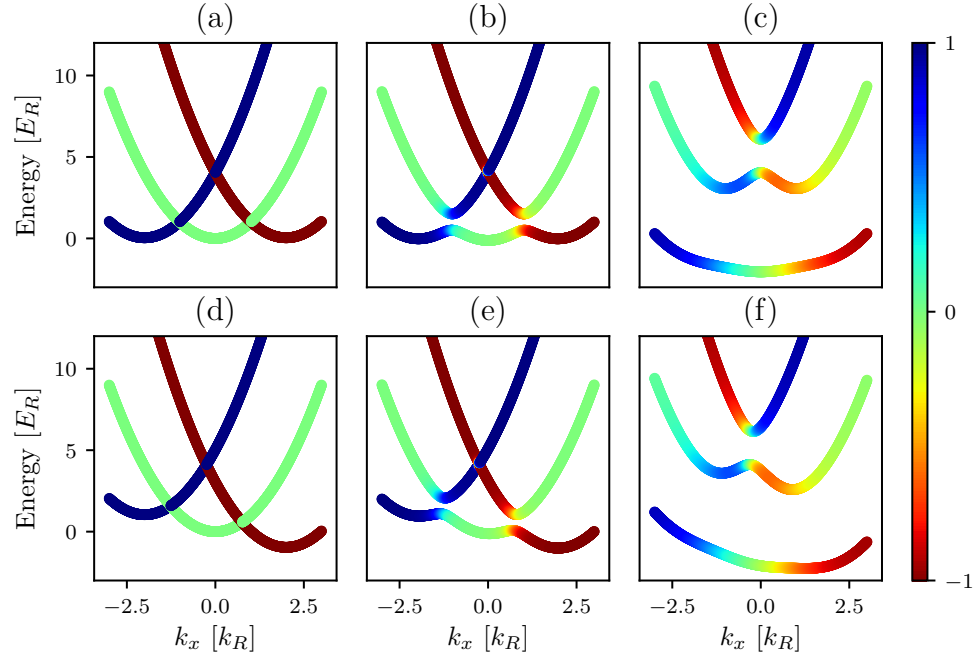


Figure 9: Band structure of the Raman Hamiltonian, Eq. 3.31, in momentum space. For all plots, the quadratic Zeeman shift  $\hbar\epsilon = 0.04E_R$ , and the color represents magnetization, labeled by the colorbar. (a)  $\hbar\Omega = 0$ ,  $\hbar\delta = 0$ . (b)  $\hbar\Omega = 1.0E_R$ ,  $\hbar\delta = 0$ . (c)  $\hbar\Omega = 5.0E_R$ ,  $\hbar\delta = 0$ . (d)  $\hbar\Omega = 0.0$ ,  $\hbar\delta = 1.0E_R$ . (e)  $\hbar\Omega = 1.0E_R$ ,  $\hbar\delta = 1.0E_R$ . (f)  $\hbar\Omega = 5.0E_R$ ,  $\hbar\delta = 1.0E_R$ .

an rf coupling field for atoms in the  $F = 1$  and  $F = 2$  manifold, respectively. The Stern-Gerlach gradient pulse separates the spin components along the horizontal axis in the images. The fractional population in each state can then be obtained by summing up the optical depth in each cloud and dividing by the total optical depth. Similarly, Figure 11a shows an example time-of-flight image obtained when pulsing on a Raman coupling field on an  $F = 1$  cloud initially in the  $m_F = 0$  spin state. Here, the spin states are separated along the horizontal axis by the same Stern-Gerlach pulse. In addition, the recoil momentum obtained when undergoing a Raman transition separates the different spin states along the vertical axis—parallel to the Raman beams along  $\mathbf{e}_x$ . The direction of the Stern-Gerlach gradient was chosen purposefully to be perpendicular to the Raman direction  $\mathbf{e}_x$  for easy separation of the two effects.

These population oscillations can then be fit for coupling strength  $\hbar\Omega$  and detuning  $\hbar\delta$ . Note that the quadratic Zeeman shift  $\hbar\epsilon$  is set by the strength of the bias field  $B_0$  and therefore often well known - we do not fit for this. The theoretic predictions are obtained by applying the time evolution operator  $U = \exp(-iH_{\text{Raman/rf}}t/\hbar)$  to an initial state  $\Psi$  in the appropriate basis. Figure 10c shows an example time series of rf pulsing in the  $F = 1$  manifold, starting in the  $m_F = 0$  state. The lines of best fit are overlayed on experimental data, extracting fit parameters  $\hbar\Omega = 0.863 \pm 0.004E_R$  and  $\hbar\delta = -0.198 \pm 0.007E_R$ . Figure 10d shows an example time series of rf pulsing in the  $F = 2$  manifold, starting in the  $m_F = -2$  state. Here, the extracted fit parameters were  $\hbar\Omega = 1.000 \pm 0.002E_R$  and  $\hbar\delta = -0.061 \pm 0.001E_R$ .

Figure 11b shows an example time series of Raman pulsing in the  $F = 1$  manifold, starting in the  $m_F = 0$  state, with fitted parameters  $\hbar\Omega = 1.47 \pm 0.01E_R$  and  $\hbar\delta = 0.004 \pm 0.024E_R$ . Note that although the coupling strength is almost double the rf coupling strength in Figure 10c, the contrast (peak to peak oscillation

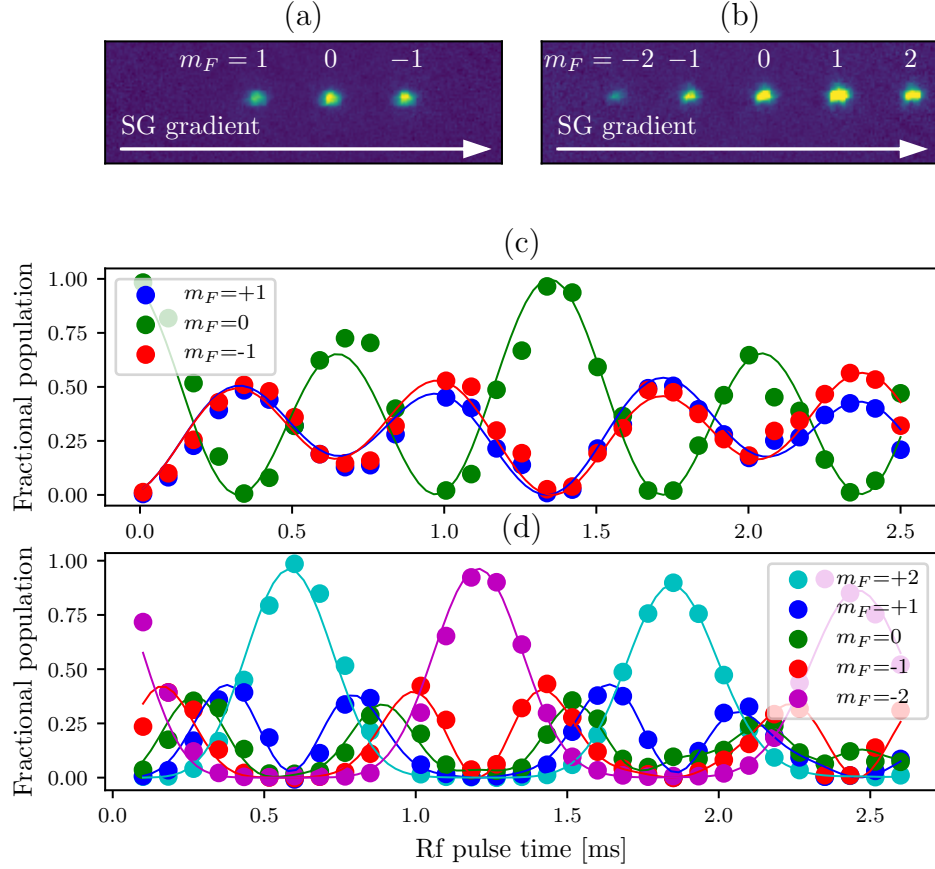


Figure 10: Pulsing on rf coupling. (a) Example time-of-flight image during an rf pulsing experiment in the  $F = 1$  manifold. Spin states are separated via a Stern-Gerlach pulse along the horizontal direction. (b) Example time-of-flight image during an rf pulsing experiment in the  $F = 2$  manifold. Here, 5 spin components are present. (c) Pulsing experiment in the  $F = 1$  manifold. Dots represent fractional populations in different spin states measured from time-of-flight images, and lines represent best fit theory curves. Fitted parameters are  $\hbar\Omega = 0.863 \pm 0.004E_R$ ,  $\hbar\delta = -0.198 \pm 0.007E_R$ . (d) Pulsing experiment in the  $F = 2$  manifold. Dots represent fractional populations in different spin states measured from time-of-flight images, and lines represent best fit theory curves. Fitted parameters are  $\hbar\Omega = 1.000 \pm 0.002E_R$ ,  $\hbar\delta = -0.061 \pm 0.001E_R$ .  $\hbar\epsilon = 0.038E_R$  for all panels.

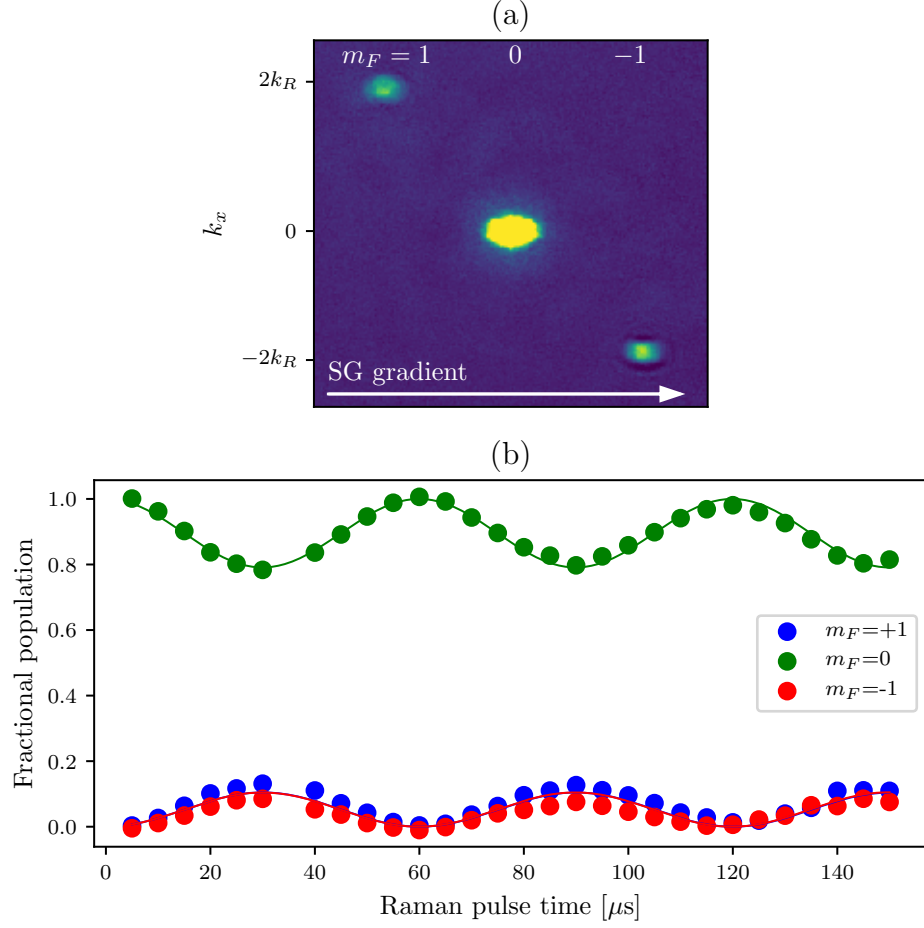


Figure 11: Pulsing on Raman coupling. (a) Example time-of-flight image during a Raman pulsing experiment in the  $F = 1$  manifold. A Stern-Gerlach pulse during time-of-flight separates different spin components along the horizontal direction, and different momentum orders fly apart along the vertical direction. (b) Fractional population in different spin states during a Raman pulsing experiment as a function of time. Dots represent data and lines represent a best fit from theory. The fitted parameters are  $\hbar\Omega = 1.47 \pm 0.01E_R$ ,  $\hbar\delta = 0.004 \pm 0.024E_R$ . The quadratic Zeeman shift was  $\hbar\epsilon = 0.038E_R$ .

of the fractional population in, say, the  $mF = 0$  state) is much lower in the Raman data than in the rf. This is a direct consequence of the recoil momentum transfer, and can be understood by looking at the band structure. For rf, the coupled bands at initial momentum  $k_x = 0$  are separated by the coupling strength, see Figure ??b. For Raman, even at zero coupling strength, due to the shifting of the parabolas by  $2k_R$ , and  $k_x = 0$  the higher bands are  $\hbar^2(2k_R)^2/2m = 4E_R$  separated from the lower bands. Therefore, the energy difference is larger and the fraction in the excited band will be lower, leading to lower contrast.

## Bibliography

- [1] Daniel Adam Steck. Rubidium 87 d line data. Available online, <http://steck.us/alkalidata>, April 2018. revision 2.1.5.
- [2] K. Jiménez-García, L. J. LeBlanc, R. A. Williams, M. C. Beeler, A. R. Perry, and I. B. Spielman. Peierls substitution in an engineered lattice potential. *Phys. Rev. Lett.*, 108:225303, May 2012.
- [3] C.J. Pethick and H. Smith. *Bose-Einstein Condensation of Dilute Gases*. Cambridge University Press, Cambridge, UK, 2002.
- [4] M. Egorov, B. Opanchuk, P. Drummond, B. V. Hall, P. Hannaford, and A. I. Sidorov. Measurement of  $s$ -wave scattering lengths in a two-component bose-einstein condensate. *Phys. Rev. A*, 87:053614, May 2013.
- [5] H.J. Metcalf and P. van der Straten. *Laser Cooling and Trapping*. Graduate Texts in Contemporary Physics. Springer New York, 1999.
- [6] N.W. Ashcroft and N.D. Mermin. *Solid State Physics*. Saunders College, Philadelphia, 1976.

- [7] Nicola Marzari, Arash A. Mostofi, Jonathan R. Yates, Ivo Souza, and David Vanderbilt. Maximally localized wannier functions: Theory and applications. *Rev. Mod. Phys.*, 84:1419–1475, Oct 2012.
- [8] Karina Jimenez-Garcia. *Artificial Gauge Fields for Ultracold Neutral Atoms*. PhD thesis, Joint Quantum Institute, National Institute of Standards and Technology, and the University of Maryland, 2012.
- [9] Daniel Adam Steck. Quantum and atom optics. Available online at <http://steck.us/teaching>, January 2015. revision 0.12.2.
- [10] Lindsey J. LeBlanc. *Exploring many-body physics with ultracold atoms*. PhD thesis, University of Toronto, 2011.
- [11] K. v. Klitzing, G. Dorda, and M. Pepper. New method for high-accuracy determination of the fine-structure constant based on quantized hall resistance. *Phys. Rev. Lett.*, 45:494–497, Aug 1980.
- [12] D. J. Thouless, M. Kohmoto, M. P. Nightingale, and M. den Nijs. Quantized hall conductance in a two-dimensional periodic potential. *Phys. Rev. Lett.*, 49:405–408, Aug 1982.
- [13] Douglas R. Hofstadter. Energy levels and wave functions of bloch electrons in rational and irrational magnetic fields. *Phys. Rev. B*, 14:2239–2249, Sep 1976.
- [14] M. C. Geisler, J. H. Smet, V. Umansky, K. von Klitzing, B. Naundorf, R. Ketzmerick, and H. Schweizer. Detection of a landau band-coupling-induced rearrangement of the hofstadter butterfly. *Phys. Rev. Lett.*, 92:256801, Jun 2004.
- [15] B. Hunt, J. D. Sanchez-Yamagishi, A. F. Young, M. Yankowitz, B. J. LeRoy, K. Watanabe, T. Taniguchi, P. Moon, M. Koshino, P. Jarillo-Herrero, and R. C.



Ashoori. Massive Dirac Fermions and Hofstadter Butterfly in a van der Waals Heterostructure. *Science*, 340:1427, 2013.

- [16] P. Zoller D. Jaksch. Creation of effective magnetic fields in optical lattices: the hofstadter butterfly for cold neutral atoms. *New Journal of Physics*, 5(1):56, 2003.
- [17] M. Aidelsburger, M. Atala, M. Lohse, J. T. Barreiro, B. Paredes, and I. Bloch. Realization of the hofstadter hamiltonian with ultracold atoms in optical lattices. *Phys. Rev. Lett.*, 111(18):185301–, October 2013.
- [18] Hirokazu Miyake, Georgios A. Siviloglou, Colin J. Kennedy, William Cody Burton, and Wolfgang Ketterle. Realizing the harper hamiltonian with laser-assisted tunneling in optical lattices. *Phys. Rev. Lett.*, 111:185302, Oct 2013.
- [19] Gregor Jotzu, Michael Messer, Remi Desbuquois, Martin Lebrat, Thomas Uehlinger, Daniel Greif, and Tilman Esslinger. Experimental realization of the topological haldane model with ultracold fermions. *Nature*, 515(7526):237–240, Nov 2014.
- [20] M Aidelsburger, M Lohse, C Schweizer, M Atala, J T Barreiro, S Nascimbène, N. R. Cooper, I. Bloch, and N. Goldman. Measuring the Chern number of Hofstadter bands with ultracold bosonic atoms. *Nature Physics*, 11(2):162–166, December 2014.
- [21] M. Mancini, G. Pagano, G. Cappellini, L. Livi, M. Rider, J. Catani, C. Sias, P. Zoller, M. Inguscio, M. Dalmonte, and L. Fallani. Observation of chiral edge states with neutral fermions in synthetic hall ribbons. *Science*, 349(6255):1510–, Sep 2015.
- [22] M Hafezi, S Mittal, J Fan, A Migdall, and J M Taylor. Imaging topological edge states in silicon photonics. *Nat. Photon.*, 7(12):1001–1005, October 2013.

- [23] A. Celi, P. Massignan, J. Ruseckas, N. Goldman, I.B. Spielman, G. Juzeliunas, and M. Lewenstein. Synthetic gauge fields in synthetic dimensions. *Phys. Rev. Lett.*, 112(4):043001–, Jan 2014.
- [24] B. K. Stuhl, H.-I. Lu, L. M. Ayccock, D. Genkina, and I. B. Spielman. Visualizing edge states with an atomic bose gas in the quantum hall regime. *Science*, 349(6255):1514–, Sep 2015.
- [25] Y. Aharonov and D. Bohm. Significance of electromagnetic potentials in quantum theory. *Phys. Rev.*, 115:485, 1959.
- [26] Yakir Aharonov and Ady Stern. Origin of the geometric forces accompanying berry’s geometric potentials. *Phys. Rev. Lett.*, 69(25):3593–3597, 1992.
- [27] Dario Hgel and Beln Paredes. Chiral ladders and the edges of quantum Hall insulators. *Phys. Rev. A*, 89(2):023619, 2014.